International Journal of Thermophysics (2022) 43:91
https://doi.org/10.1007/s10765-022-03010-3

ADVANCED SPACECRAFT MATERIALS

Advanced Passive Thermal Control Materials and Devices for Spacecraft: A Review

Sumitaka Tachikawa[1] · Hosei Nagano[2] · Akira Ohnishi[1] · Yuji Nagasaka[3]

Received: 24 February 2022 / Accepted: 16 March 2022 / Published online: 21 April 2022

Abstract

In recent planetary exploration space missions, spacecraft are exposed to severe thermal environments that are sometimes more extreme than those experienced in earth orbits. The development of advanced thermal control materials and devices together with reliable and accurate measurements of their thermophysical properties are needed for the development of systems designed to meet the engineering challenges associated with these space missions. We provide a comprehensive review of the state-of-the-art advanced passive thermal control materials and devices that are available for space applications, specifically, variable emissivity thermal control materials and microelectromechanical systems (MEMS), radiofrequency (RF)-transparent and/or tunable solar absorptivity and total hemispherical emissivity thermal control materials, and a passive re-deployable radiator with advanced materials and insulation. Prior to our in-depth review of these thermal control materials, we briefly summarize the thermal environments surrounding spacecraft, the characteristics of thermophysical properties for spacecraft materials that differ from those of materials for ground use, and the significance of solar absorptivity and total hemispherical emissivity for passive thermal control in space. In all four topics of materials and devices, the following subjects are overviewed: the basic principle of passive thermal control techniques in space, the measurement of thermophysical properties of those novel materials, simulation and/or on-orbit verification thermal performance tests, degradation tests in space environments, and some aspects of the implementation of the above-described materials and devices in actual space missions.

Keywords Emissivity · $La_{1-x}Sr_xMnO_3$ · Multilayer insulation · Polyimide form · Pyrolytic graphite sheet · Solar absorptivity · Thermal conductivity · Variable emissivity material

This article is part of the Special Issue on Thermophysics of Advanced Spacecraft Materials and Extraterrestrial Samples.

✉ Yuji Nagasaka
nagasaka@sd.keio.ac.jp

Extended author information available on the last page of the article

1 Introduction

Many indispensable technologies that maintain the temperatures of systems within allowable limits are used in our daily lives; for example, cooling fans and heat pipes are vital components to reject the Joule heating generated from the semiconductor chips compacted into the small space of a laptop computer. To maintain comfortable temperatures in homes and work settings during the summer and winter, we use air-conditioning systems that use the latent heat of the liquid–gas phase change of refrigeration fluid. The walls of a refrigerator are composed of thermal insulation to keep the inside temperature low, reduce the power consumption as much as possible, and minimize the emission of CO_2. All of these terrestrial mechanisms of heat transfer, i.e., conduction, convection, and radiation, are well known, and their fundamental principles remain unchanged [1–3].

In contrast, in high-vacuum extraterrestrial environments, the heat transfer between a spacecraft and its surrounding space is governed only by radiation. It may thus seem trivial to search for optimal solutions in principle for thermal control problems that exist in space. However, when thermal control design is conducted under the strict constraints of making a spacecraft as light as possible and with as little energy consumption as possible, the importance of new passive thermal control materials and devices emerges. In this research field, the thermophysical properties of materials (i.e., the total hemispherical emissivity, solar absorptivity, and thermal conductivity) dominate the performance of the system, and in fact these properties are significantly more dominant than in heat transfer devices on the ground. There is a frontier of engineering thermophysical properties research and system design at which a device itself cannot be established without newly designed materials and accurate values of their thermophysical properties.

The research frontier of this field of thermophysics has been driven by the present and planned planetary exploration space missions, in which spacecraft are exposed to a wide range of thermal environments, some of which are more extreme than those experienced in Earth's orbit. There are several examples of such missions. The ESA-JAXA (European Space Agency-Japan Aerospace Exploration Agency) joint mission to Mercury consists of two spacecraft [Mercury Planetary Orbiter [MPO] and Mercury Magnetosphere Orbiter (MMO)] that are exposed to extremely strong solar radiation [4]. Ultimately, NASA's Parker Solar Probe is experiencing the most severe thermal environment, traveling directly through the atmosphere of the Sun [5]. Other challenges would accompany explorations to the edge of our solar system, e.g., Pluto, which receives less than 0.1 % of Earth's solar radiation [6]. Additional examples are the recent planetary exploration missions under unprecedented thermal environments and the sample return missions associated with Hyabusa2 [7], OSIRES Rex [8], and MMX [9].

This review focuses on advanced passive thermal control materials and devices among spacecraft thermal control technologies, where thermophysical properties and their changes dominate with no-energy-consumption device design. We will introduce and review the basic principles of passive thermal control in space; the

measurement of the thermophysical properties of the novel materials employed; degradation tests against ultraviolet (UV) radiation, atomic oxygen, protons, and electrons in a real or simulated space environment (in other words, the long-term durability of materials in space); and some implementation examples for actual space missions.

2 Thermal Environments Surrounding Spacecraft

Spacecraft are exposed to very different thermal environments over the course of their launch from the earth, their various missions in outer space, and possibly their return to Earth. The thermal environments experienced by spacecraft in each phase are distinctly classified into the following four categories: (1) Earth orbit environments, (2) interplanetary orbit environments, (3) launch environments, and (4) re-entry into Earth's or another planet's atmosphere [10–12]. Spacecraft's thermal control systems are usually designed for the thermal environments that are encountered during missions within the Earth's orbit [10], where the atmospheric environment is characterized by a high vacuum; the atmospheric pressure above 300 km from the Earth's surface is 10^{-7} hPa or less [11]. In the thermal environments of categories (1) earth orbit and (2) interplanetary orbit, aerodynamic heating and convective heat transfer to the spacecraft can therefore be ignored.

The thermal design strategies against aerodynamic heating require special designs, e.g., a fairing to protect the spacecraft during launch, and the use of heat-resistant protective material and/or ballistic re-entry capsules for re-entry. References [10–12] provide typical examples of thermal design regarding (3) launch and (4) re-entry thermal environments. This review deals with the thermal environments surrounding spacecraft in categories (1) earth orbit and (2) interplanetary orbit.

Figure 1 illustrates the thermal environments surrounding a spacecraft for (1) a planetary (Earth) orbit and (2) an interplanetary orbit. In the figure, $J_S(d)$ is the solar radiation intensity at distance d (astronomical unit: au) from the sun in $W{\cdot}m^{-2}$, $J_A(W{\cdot}m^{-2})$ is the albedo which is expressed as the fraction of the incident solar radiation reflected from the nearby planet (Earth), and $J_P(W{\cdot}m^{-2})$ is the infrared (IR) radiation emitted from the nearby planet (Earth). These radiation intensities are described in some detail below.

2.1 Solar Radiation Intensity

Solar radiation is the heat flux that a spacecraft receives directly from the sun, and it is the largest source of external heating. As is well known, the spectral distribution of solar radiation is quite similar to that of a blackbody radiation at 5780 K [13] and peaks at 0.48 μm. For the thermal design of a spacecraft traveling to outer planets of our solar system including Earth, it is sufficient to consider the wavelength region of 0.25 μm to 2.6 μm in which 98 % of the total solar radiation flux exists [12]. However, in the case of the inner planets such as Mercury and Venus, a wider range including both shorter and longer wavelengths

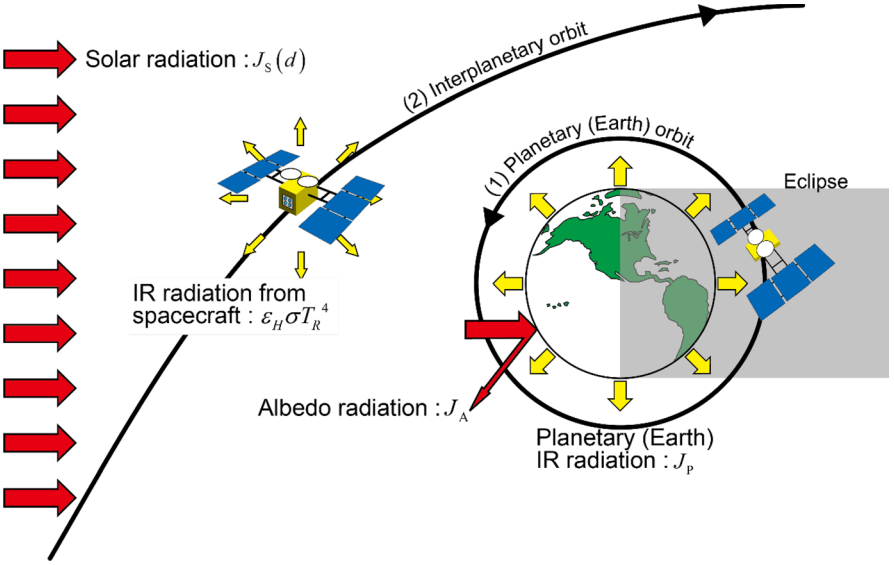

Fig. 1 Thermal environments surrounding spacecraft for (1) a planetary (Earth) orbit, and (2) an interplanetary orbit. The cosmic background radiation intensity corresponding to about 2.7 K blackbody radiation is extremely small compared to the solar radiation intensity and can be ignored here

must be taken into consideration. The solar radiation intensity immediately outside the Earth's atmosphere is called the solar constant, which is 1367 $\mathrm{W{\cdot}m^{-2}}$ at the earth's average distance (astronomical unit: 1au) from the sun [10]. In an interplanetary orbit, the solar radiation intensity is inversely proportional to the square of the distance from the sun and can be expressed by the following equation in au units [10].

$$J_S(d) = \frac{1367.5}{d^2} \quad \mathrm{W \cdot m^{-2}}, \tag{1}$$

where $J_S(d)$ is the solar radiation intensity at distance d (astronomical unit: au) from the sun.

Table 1 lists the equatorial radius in km, the orbit semimajor axis in au, the solar radiation intensity values relative to Earth calculated using Eq. 1, and the albedo coefficient of the planets of our solar system and Earth's moon [10, 11]. For a thermal engineer, it is important to note that the solar intensity is continuously monitored; the average values of the solar constant are determined annually and announced later, and these values have been estimated to be accurate within ± 0.4 % [10, 14]. In the orbit around the Earth, the solar constant is the maximum value of solar radiation intensity which is received by the surface of a spacecraft perpendicular to the solar radiation during the daytime. For detailed thermal designs, it is necessary to consider the solar incidence angle on each surface of a spacecraft over the course of a day plus sudden changes in the incident angle between day (maximum value) and night (eclipse time, essentially zero); however, this topic is the beyond the scope of this review [10].

Table 1 Planetary solar radiation intensity relative to Earth values at 1 au and albedo. Reproduced by courtesy of Aerospace Corporation, Table 1.1 [10] and by permission from John Wiley and Sons, Table 11.2 [11], Copyright (2022)

Planet	Equatorial radius (km)	Orbit semimajor axis in astronomical unit (au)	Solar radiation intensity, $J_s(d)$ calculated by Eq. 1 and tabulated as a percentage of solar intensity at 1au	Planetary albedo (–)
Mercury	2425	0.3871	667	0.06 to 0.10
Venus	6070	0.7233	191	0.60 to 0.76
Earth	6378	1.000	100	0.31 to 0.39
Moon	1738	1.000	100	0.07
Mars	3397	1.524	43.1	0.15
Jupiter	71 300	5.20	3.70	0.41 to 0.52
Saturn	60 100	9.54	1.10	0.42 to 0.76
Uranus	24 500	19.18	0.27	0.45 to 0.66
Neptune	25 100	30.06	0.11	0.35 to 0.62
Pluto	3200	39.44	0.064	0.16 to 0.40

1 au (Astronomical unit): is defined by the IAU (International Astronomical Union) as exactly = 149 597 870 700 m [118], which is approximately the average distance between the earth and the sun

2.2 Albedo Radiation Intensity

A planet's albedo radiation intensity J_A is the fraction of the solar radiation intensity that is scattered from the surface and atmosphere of a nearby planet. Table 1 provides the approximate albedo for the planets [11]. The intensity of albedo radiation depends on the size of a planet, the reflective properties of the planet's surface, the atmosphere of the planet, and the altitude and orbit of the spacecraft; the albedo radiation intensity is also highly variable [10]. Accurate information about an albedo is required, particularly for spacecraft flying in low planetary orbit (low Earth orbit [LEO]) and during touchdown operations. Reference [15] provides more detailed information about the albedo of Earth.

2.3 Planetary IR Radiation Intensity

Although the incident solar radiation is partly reflected as an albedo, the rest of the energy is eventually absorbed by a planet and emitted from the planet's surface to space as IR radiation $\varepsilon_H \sigma T^4$ because the temperature of the planet is relatively low. In the case of Earth, the effective average temperature is about 255 K (the Earth's IR radiation intensity is calculated to be 240 $W \cdot m^{-2}$ assuming $\varepsilon_H = 1$) so that the wavelength of the IR emission spectrum is 2–50 μm with the peak wavelength of ~ 10 μm. The IR radiation is as important in touchdown operations to planets as the albedo, for example, it is especially important in the cases of touchdown to asteroids with high surface temperature; here, the IR radiation has a greater effect than the albedo.

3 Characteristics of the Thermophysical Properties for Spacecraft Materials That Differ from Those in Ground Use

When we deal with the thermophysical properties of spacecraft materials, there are two major differences compared to the properties of materials that are used on the ground.

3.1 Degradation of Thermophysical Properties of Spacecraft Materials Caused by Space Environmental Factors Such as UV Radiation, Atomic Oxygen, Protons, and Electrons

A variety of materials from metals to polymers are used in spacecraft, and these materials are strongly affected by environmental factors in space that differ from those on the Earth's surface. In particular, thermal control materials used on the external surface of spacecraft are directly exposed to many space environmental factors (such as UV radiation, atomic oxygen, protons, and electrons) which hardly reach the surface of the Earth due to the shielding provided by the Earth's atmosphere, including the ozone layer. The net effect of these space

environmental factors on spacecraft materials is to degrade the optical, thermal, electrical, and mechanical properties of the material.

For example, UV radiation in the wavelength range below 290 nm does not reach the surface of the Earth. However, in space, UV radiation—especially in the wavelength range 10–200 nm—has energy that is high enough to change the chemical bond structure of polymers, and it thus makes materials brittle. A material's exposure to UV radiation also changes the material's resistivity and thereby affects the material's thermal and optical properties. For more details regarding space environments' effects on materials, see References [10–12].

In the thermal design of a spacecraft, not only the thermophysical properties at the initial stage of launch (beginning of life [BOL] values) but also those at the end of the operation (end of life [EOL] values) must be determined and addressed. As explained above, the thermal control materials on the outermost parts of a spacecraft are affected by the harsh space environment, which degrades the value of thermophysical properties [10, 12]. If this degradation behavior is not quantitatively understood, the thermal designer will be obliged to set the design margins larger than necessary in order to guarantee the performance of the spacecraft at the end of the operation, which will lead to increases in the spacecraft's size, weight, and costs. In other words, if the amount of degradation cannot be grasped in advance, a thermal designer will not know the numerical values to be used for the thermophysical properties, and the design will not move forward. From the viewpoint of thermophysics, the thermophysical properties of a material are usually considered to be a constant at the same temperature and pressure. However, in the case of spacecraft thermal control materials, it is reasonable from an engineering standpoint to expect that the thermophysical properties will change because the material degrades in a space environment over long periods, e.g., months or years.

Naturally, the thermophysical properties of materials used in space must be measured on the ground in a high vacuum and over a wide temperature range. Moreover, to verify whether the newly developed thermal control materials are sufficiently resistant to the environment in the planned orbit (i.e., changes in the thermophysical properties are sufficiently small), exposure tests in a simulated space environment created by a ground test apparatus are always carried out in advance [12]. Although it seems to be a contradiction, it should be noted that an orbital environment cannot be completely simulated in a ground test experiment in terms of exposure time and irradiation intensities. For example, Iwata et al. reported the recovery of the degradation of proton-irradiated polymer films [16, 17]. This recovery phenomenon is thought to occur because the lifetime of radiation-generated radicals in the polymer films (which cause the increase in solar absorptivity) is from a few weeks to a few months.

3.2 Significant Differences in Usage Patterns and Weight Restrictions of Materials from the Ground

- Spacecraft are usually used only once, and maintenance is not possible during a spacecraft's operation except for very rare cases, i.e., the Hubble Space Telescope and the International Space Station.

- Due to the very high launch cost constraints, the weight and size of the spacecraft must be reduced as much as possible.

The thermal control of a spacecraft involves keeping all of the components of the spacecraft within the allowable temperature limits in all operating modes and in all space environments. There are two types of thermal control for spacecraft: active thermal control using heat pipes and heaters, etc., and passive thermal control with the conventional use of louvers, multilayer insulation (MLI), and optical solar reflectors (OSRs). It can be said that the thermal control technology of spacecraft has reached a certain level of maturity as one of the basic technologies for achieving conventional-level missions [10, 12]. However, with the continued expansion and sophistication of space development and utilization, the density of the heat generation inside the spacecraft will increase and the spacecraft will be exposed to more severe thermal environments, and thus the thermal control of spacecraft has become more important than ever. The reductions of the weight and size of the spacecraft and the energy required for thermal control are also important from the viewpoint of launch costs.

4 Passive Thermal Control Materials and Devices, and the Radiative Properties α_S and ε_H

Figure 2 is a simplified representation of the steady state thermal balance in the radiator cross-section of a spacecraft. The spacecraft can be modeled as being connected to space through the external surfaces of the radiator. It is also assumed that the radiator is isothermal and the inside surfaces are thermally insulated except for the surface that is connected to the heat-dissipating equipment. As described in the previous section, the heat inputs from space to the spacecraft are the solar radiation intensity J_{S}, the albedo radiation intensity J_{A}, and the planetary IR radiation intensity J_{P}; these radiations are received by the radiator of the surface area A_R (m^2). Another energy input is from the internal equipment power dissipation, denoted as $\dot{Q}_{\mathrm{int}}$ (W). The heat output from the spacecraft to space is the IR radiation intensity $\varepsilon_H \sigma T_R{}^4$ from the radiator surface. Assuming that the total hemispherical emissivity (emittance) of the radiator surface is ε_H and that of the solar absorptivity (absorptance) is α_S, the following thermal balance equation holds in the steady state.

$$\alpha_S J_{\mathrm{S}} A_R + \alpha_S J_{\mathrm{A}} A_R + \varepsilon_H J_{\mathrm{P}} A_R + \dot{Q}_{\mathrm{int}} = \varepsilon_H \sigma T_R^4 A_R \ (\mathrm{W}), \tag{2}$$

where σ represents the Stefan–Boltzmann constant (5.670×10^{-8} $\mathrm{W \cdot m^{-2} \cdot K^{-4}}$). This equation means that the temperature of the radiator rises due to the absorbed radiant energy, but at the same time, the emission of IR thermal radiation to space rises due to the temperature increase of the radiator itself, which is proportional to the fourth power of temperature, and the input and output energies are balanced at the steady-state temperature T_R (K). For the sake of convenience, in the case of an interplanetary orbit with no internal power dissipation, Eq. 2 can be expressed as follows:

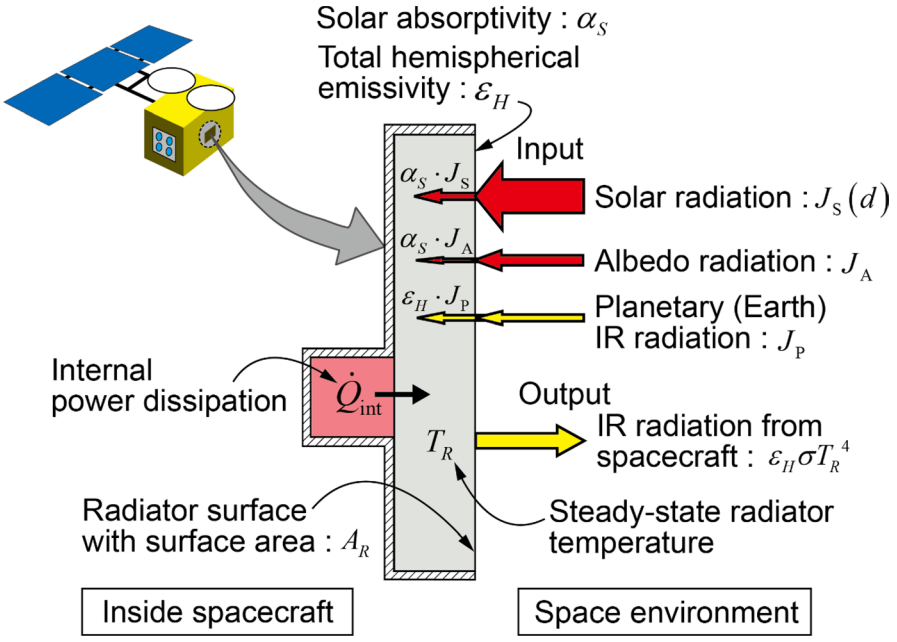

Fig. 2 The thermal balance at steady-state of a radiator in a space environment

$$T_R = \left(\frac{J_S}{\sigma} \frac{\alpha_S}{\varepsilon_H} \right)^{1/4} \tag{3}$$

In other words, since J_S and σ are constants, the temperature of the radiator (or the spacecraft) can be controlled by varying the ratio of the radiative properties of the outer surface α_S/ε_H. It can be considered that the relationship of $T_R \propto (\alpha_S/\varepsilon_H)^{1/4}$ essentially holds even when the internal power dissipation exists and/or the area(s) receiving radiation differ for each component. It should be mentioned here that in the case of the planetary orbit, J_S is sufficiently assumed to be constant (zero in the solar eclipse) during the mission, whereas in the interplanetary orbit, $J_S(d)$ changes significantly depending on the distance from the sun as expressed by Eq. 1. As a consequence, a radiator (or more generally a thermal control device) that can respond to large changes in the thermal radiation input during the mission period is required.

As is well known, at a given wavelength λ in all wavelength regions, $\alpha(\lambda)$ and $\varepsilon(\lambda)$ of any material surface are equal according to Kirchhoff's law. In the space radiation environment, fortunately, the input thermal radiation related to the absorptivity is basically in the visible light wavelength region, whereas the output thermal radiation associated with the emissivity is in the IR wavelength region. It is therefore possible to change α_S and ε_H independently on a single material surface.

The fundamental principle of the passive thermal control of spacecraft is based on the asymmetry of the absorption in the visible wavelength region with the

emission in the IR wavelength region on the material surface. We are able to achieve thermal control of spacecraft by selecting the appropriate materials with α_S/ε_H values that are suitable for the space thermal environment of a particular mission. Figure 3 shows the mapping of α_S and ε_H ranges of various materials conventionally used in spacecraft thermal control. The various materials and coatings indicated in this figure have been used for many years, and the need to develop new materials is not high for conventional missions [10]. In order to make it easier for the reader to understand the significant effect of α_S/ε_H, we will present a simple calculation example using Eq. 3. When receiving the maximum solar radiation in the orbit around the earth, $T_R = 394$ K at $\alpha_S/\varepsilon_H = 1$ (black body), while it is possible to set a safe $T_R = 294$ K by selecting an appropriate $\alpha_S/\varepsilon_H = 0.31$ (e.g., for white paint). However, it is necessary to bear in mind that the closer the spacecraft is to the sun, the closer that the α_S must be to zero in order to maintain it near $T_R = 300$ K, and thus in reality, the thermal control by this method alone reaches its limit.

4.1 Variable Emissivity Thermal Control Materials and MEMS

As expressed in Eq. 3, the temperature of an object in space is essentially determined by the ratio of the solar absorptivity α_S to the total hemispherical emissivity ε_H of the outer wall surface. If the thermal environment around the spacecraft is always constant, the spacecraft can be kept at the target constant temperature by using materials with appropriate α_S/ε_H values. However, in reality, the direction and amount of the solar heat flux to the spacecraft's surfaces change with time, and it

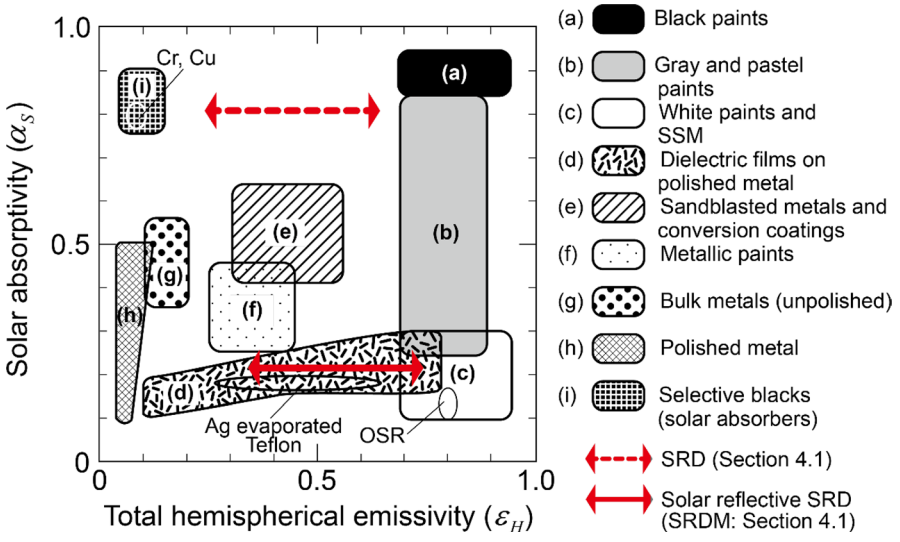

Fig. 3 The total hemispherical emissivity and solar absorptivity values for various conventional passive thermal control materials and a smart radiation device (SRD) for spacecraft. Reprinted by courtesy of Aerospace Corporation, Fig. 4.2 in [10] and Fig. 4.4.1 in [12], SSM: second-surface mirror

is thus common to cover a spacecraft with a heat-insulating material in order to prevent the spacecraft from undergoing changes in the space thermal environment. On the other hand, if the entire spacecraft is covered with a heat-insulating material, the heat generated by the internal equipment cannot be rejected. Therefore, in actual spacecraft design, a radiator surface is installed so that the temperature of the internal equipment falls below the upper limit of the allowable temperature under high-temperature conditions, and the rest of the surfaces are covered with a heat-insulating material. In contrast, under low-temperature conditions, a heater is used so that the temperature of the spacecraft does not fall below the lower limit of the allowable temperature.

A louver, which is a mechanical thermal control element, is conventionally used to reduce the heater power [10]. A louver is a device with multiple blades that can be opened or closed by using a bimetallic and spring-actuated mechanism; the louver is placed over the external radiator. When the temperature of the equipment is low, the blade with a highly polished metallic surface is closed in order to reduce the thermal coupling between space and the radiator. Conversely, when the temperature is high, the blades are opened to directly expose the radiator surface to space. However, in the case of very small satellites (which are likely to be subjected to large temperature changes due to their low heat capacity) and in the case of interplanetary spacecraft (whose distance to the sun changes significantly during the course of the mission), the traditional thermal control element technologies such as louvers and heaters, combined with the reduction of mass and size and with the minimum electrical energy consumption, are no longer sufficient to meet the requirements of the thermal design.

As a possible solution to this problem, the following method has been considered: controlling the amount of reject heat by artificially changing the emissivity of the radiator in response to the temperature of the radiator. Alternatively, if there is a material whose emissivity changes autonomously in the direction of reducing the temperature changes depending on the temperature of the spacecraft itself, there is another possible solution: passive thermal control materials for spacecraft. Materials with such functions are generally called variable emissivity materials, which are divided into electrochromic materials and thermochromic materials. There have been quite a few experimental and theoretical studies of these materials and devices. Electrochromic materials are materials whose optical properties change reversibly when a voltage is applied; typical electrochromic materials are tungsten oxide (WO_3) and polyaniline (PANI) [18]. Thermochromism is a phenomenon in which the optical properties of a substance change depending on the temperature. For the purpose of spacecraft thermal control, the characteristics of thermochromic materials whose thermal radiation property changes are induced by the metal–insulator phase transition due to temperature changes are utilized. The following is a review of IR wavelength variable emissivity materials that are primarily intended for space applications.

Consider the ideal temperature dependence of a variable emissivity material that can replace the function of the conventional louver. Devices made from that material must be lightweight and with zero power consumption, and the devices must be designed to ensure the long life and long-term reliability of the spacecraft. Figure 4

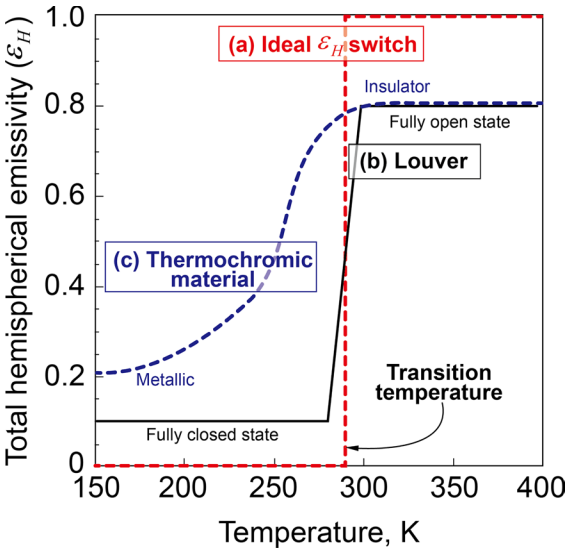

Fig. 4 Comparison of (a) an ideal total hemispherical emissivity switch, (b) a louver, and (c) a thermochromic material for spacecraft thermal control. In the case of the thermochromic material, a significant change in total hemispherical emissivity occurs due to a metal–insulator transition

illustrates the temperature dependences of the ideal total hemispherical emissivity switch, a louver, and a possible thermochromic material with similar functions. The transition temperature at which the emissivity changes must be set near room temperature because most of the electrical and mechanical equipment used in spacecraft is originally designed to operate on Earth. Therefore, the ideal emissivity switch autonomously controls the spacecraft temperature to keep it constant at the transition temperature by changing the emissivity from 0 to 1 in response to the spacecraft's temperature.

With the louvers that have been used in numerous spacecraft, the operating temperature of the bimetallic mechanism is set at room temperature. At high temperatures, the louver is in its fully open state and heat is rejected with a high emissivity radiator surface ($\varepsilon_H \sim 0.8$). At low temperatures, the louver is in its closed state to provide low emissivity ($\varepsilon_H \sim 0.1$) on the blades' surface, for heat insulation. Appropriate control of the blades' opening/closing angles can be set to an intermediate emissivity corresponding to the differential temperature of about 10°–20 °C. By such an operation, the louver has a function of reducing the temperature change of the spacecraft. However, such louvers weigh several kg to 10 kg per 1 m^2 [10]. A thermochromic material that functions as well as or better than a louver must have an electrical insulating property (high ε_H) at high temperatures and a metallic property (low ε_H) at low temperatures, centering on the transition temperature to be controlled. In addition, the material must be able to be installed on the radiator surface in a lightweight thin film or coating.

From 1998 to 2001, Shimazaki et al. focused on the phenomenon in which melt-grown crystals of $LaMnO_3$ doped with Sr cause a large change in resistivity due to a metal–insulator transition near room temperature [19–21], depending on the amount of Sr doping [22, 23] as shown in Fig. 5. They prepared polycrystalline Sr-doped lanthanum manganese oxide (LSMO) formed in the perovskite-type

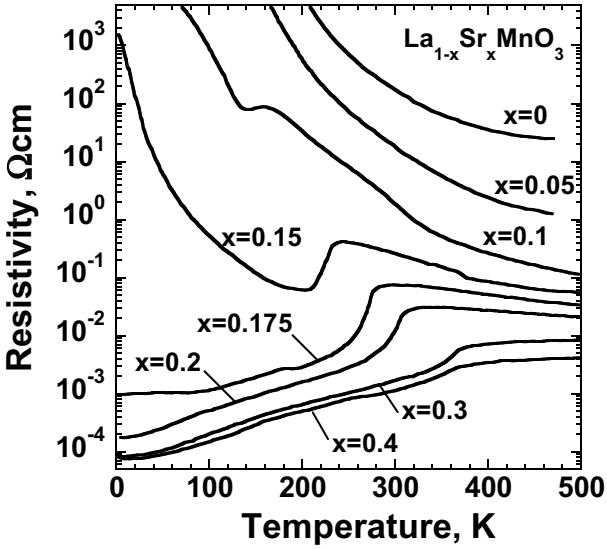

Fig. 5 The temperature dependence of electrical resistivity of melt-grown crystals $La_{1-x}Sr_xMnO_3$ measured by the conventional four-probe method. Reprinted with permission from [21] Copyright (2022) by the American Physical Society

structure $La_{1-x}Sr_xMnO_3$ (x = 0, 0.15, 0.175, 0.2, 0.3, and 0.4 samples) by the standard ceramic production process (30 × 30 × 0.2 mm), and the surfaces of every sample were polished with diamond slurry to make the root-mean square surface roughness < 30 nm [20].

Figure 6a shows the molecular structure of LSMO. The temperature dependence of the ε_H of the LSMO was measured by the calorimetric method [24] in the temperature range from 173 K to 373 K with an estimated uncertainty of ± 2.2 %. With these experimental results, Shimazaki et al. were the first to discover that $La_{0.825}Sr_{0.175}MnO_3$ showed the remarkable total hemispherical emittance change of $\Delta\varepsilon_H = 0.42$ at approx. 280 K, which is a suitable property for a thermochromic material for passive spacecraft thermal control. Figure 7 depicts the experimental results for the temperature dependence of the total hemispherical emissivity of LSMO with different Sr doping [20], which correlated with those for electrical resistivity as shown in Fig. 5. Shimazaki et al. also measured the spectral reflectance of LSMO by Fourier transform IR spectroscopy in the wavelength range of 0.25 to 100 μm at room temperature to calculate the optical constants, in order to clarify that the metal–insulator transition is due to Sr doping.

Over the years since then, the research groups led by JAXA's Ohnishi and Tachikawa have consistently conducted both fundamental studies, space environmental tests on the ground, and on-orbit verification tests to test the use of LSMO as a thermal control material for spacecraft. Shimakawa et al. [25] investigated the film thickness dependence of the emissivity property of LSMO, and they observed that 1500-nm-thick films can be used for variable emittance radiators. Ochi et al. [26, 27] developed thin and light ceramic tiles (thickness < 70 μm and weighing 450 g/m^2) of

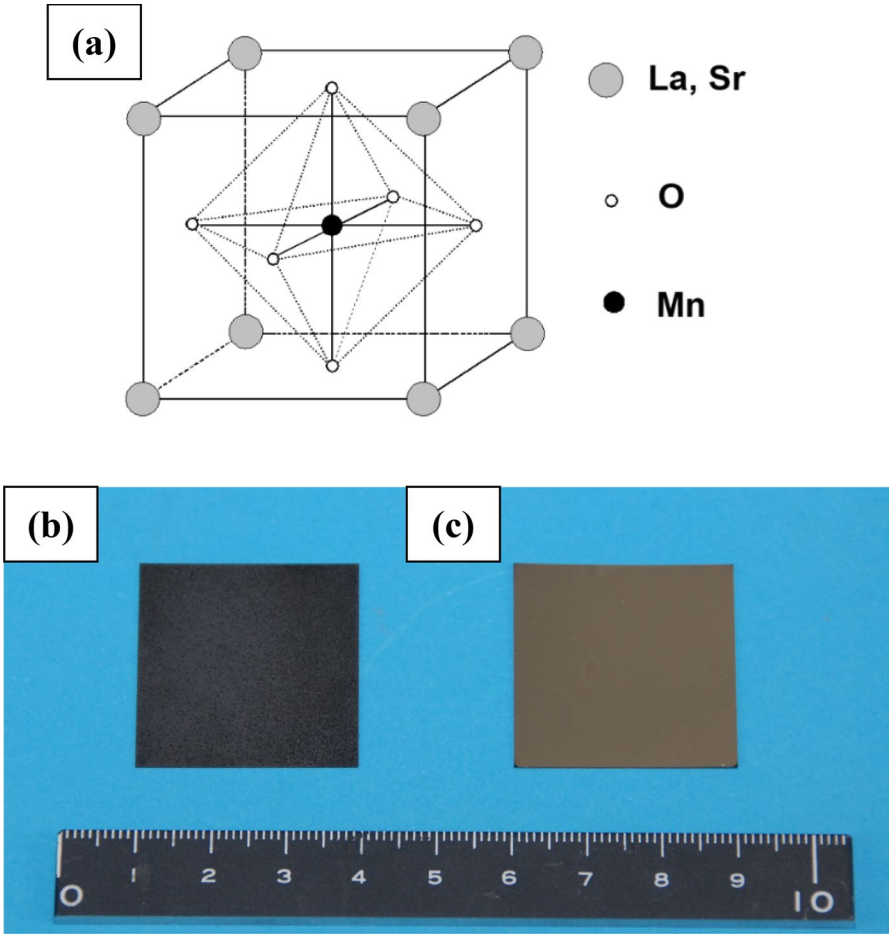

Fig. 6 (a) The molecular structure of LSMO, (b) a SRD ($La_{0.775}Sr_{0.115}Ca_{0.11}MnO_3$) sample 30 mm × 30 mm × 70 μm, and (c) a SRDM (Smart Radiation Device with Multilayer film) sample coated with a multilayer film designed by a genetic algorithm to reduce solar absorptivity ($\alpha_S = 0.24$) for use in radiators [32]

LSMO for thermal control applications on spacecraft. They named these new materials to be used in a spacecraft's variable emissivity radiator "smart radiation devices (SRDs)" [28] based on $La_{0.825}Sr_{0.175}MnO_3$ and $La_{0.7}Ca_{0.3}MnO_3$ composed of a thin and lightweight ceramic tile. They designed multilayer films for reducing the solar absorptivity of SRDs while retaining their IR-radiative properties; they also performed space environmental simulation tests on ground and in space to evaluate the optical properties of SRDs [29].

An optimal computational design method using a genetic algorithm (GA) for spectral selective multilayer films was developed to improve the high solar absorptivity that had been a drawback of SRDs' use as a radiator for spacecraft [30]. An SRD without solar reflective coating can be used as a radiator if it is installed on

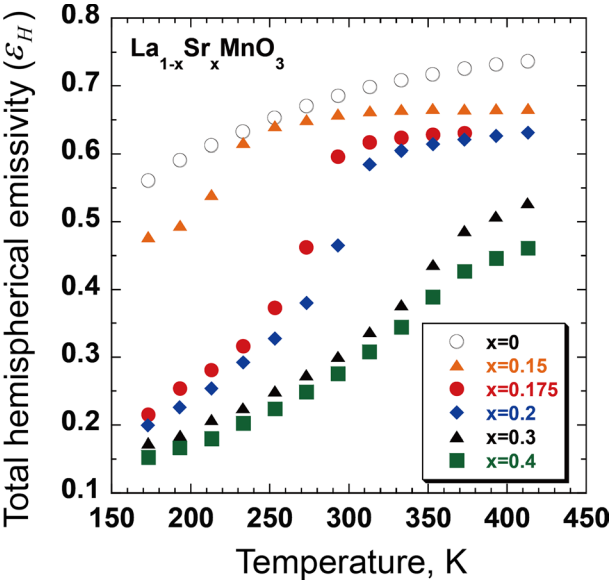

Fig. 7 Experimental results of the total hemispherical emissivity of polycrystalline $La_{1-x}Sr_xMnO_3$ ($x=0$, 0.15, 0.175, 0.2, 0.3, and 0.4) corresponding to those of electrical resistivity shown in Fig. 5. Reprinted by permission from Springer Nature [20], Copyright (2022)

the surfaces of the spacecraft that are not exposed to the solar radiation. The experimental results regarding the solar absorptivity and total hemispherical emissivity of SRDs with a multilayer film (which is evaporated on the surface of the SRD by the electron beam evaporation method) agreed well with the calculated results: by adding the multilayer film, Tachikawa et al. succeeded in reducing the solar absorptivity form 0.81 to 0.22 while maintaining the total hemispherical emissivity change ($\Delta\varepsilon_H=0.42$) as shown in Fig. 6b and 6c [31, 32] and illustrated in Fig. 3, together with other conventional passive thermal control materials.

After the above-described fundamental studies, the research group aimed at further improving the performance of SRDs (ceramic tiles) and reducing their manufacturing costs and weight [33, 34]. For an on-orbit verification test, the developed SRDs ($La_{0.775}Sr_{0.115}Ca_{0.11}MnO_3$) with an improved optical properties were mounted on the asteroid explorer "HAYABUSA" (MUSES-C) launched in May 2003 [35] and the small satellite called the innovative-technology demonstration experiment "REIMEI" (INDEX) launched in August 2005 [36]. Figure 8 exhibits the SRDs mounted on HAYABUSA under assembly. During the course on the orbit, the distance from the spacecraft to the sun varied from 0.86 au to 1.70 au, which means that the spacecraft experienced solar heat flux variation by a factor of 4. The on-orbit temperature history of the on-board SRDs demonstrated that the temperature variations of these components could be successfully minimized while saving the heater power, as expected [35].

Most of the LSMO research since 2010 has been related to their thin film manufacturing methods aimed at improving emissivity changes. These studies include the

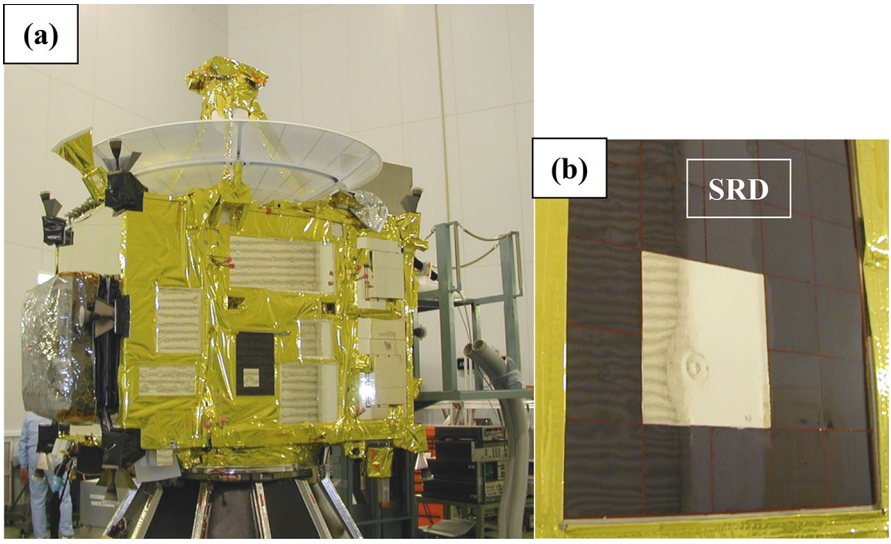

Fig. 8 (a) The SRD mounted on HAYABUSA, an asteroid explorer which was launched in May 2003, under assembly, (b) SRD (Type3 $La_{0.775}Sr_{0.115}Ca_{0.11}MnO_3$): size = 40 mm × 40 mm × 70 µm (single tile), weight = 461 g/m^2, $\varepsilon_H = 0.23$ to 0.64, and $\alpha_S = 0.81$ [12]. Since the angle of solar radiation on Hayabusa was always controlled from above (in photo (a)), there was no solar radiation on the SRD installed on the side of the structure

assessment of $La_{0.8}Sr_{0.2}MnO_3$ thin films grown on quartz glass at room temperature with the DC magnetron sputtering of an LSMO compound, followed by post-annealing [37]; LSMO films deposited on Si(100) substrates by DC magnetron sputtering followed by air annealing ($\Delta\varepsilon = 0.45$) [38]; painting-type $La_{0.8}Sr_{0.2}MnO_3$ coating with $\Delta\varepsilon > 0.3$ [39]; $Sm_{1-x}Sr_xCoO_3$ with the same perovskite-type structure as LSMO prepared by the conventional solid-state reaction method [40]; and magnetron sputtered $La_{0.7}Sr_{0.3}MnO_{3-\delta}$ films implanted with oxygen ions and various negative pulsed voltages (10–50 kV) by plasma immersion ion implantation [41]. Shen et al. studied the effect of Sr doping on the structure and emissivity of LSMOs prepared on MgO (100) substrates by pulsed laser deposition, and they obtained ($\Delta\varepsilon = 0.28$ for $La_{0.8}Sr_{0.2}MnO_3$ [42]. Wang et al. prepared dense LSMO bulk ceramics by spark plasma sintering to study the temperature dependence of these materials' transport behavior and thermochromic property as a function of the Sr concentration [43]. Liu et al. calculated the emissivity of LSMO by using a generalized gradient approximation exchange–correlation functional in the first-principles method [44].

More recently, methods of preparing LSMOs have been studied, including a coating prepared on an yttria-stabilized zirconia (YSZ) substrate by sol–gel $La_{1-x}Sr_xMnO_3$ ($x = 0.125$, 0.175, and 0.2) nanoparticles, and a binder composed of terpineol and ethyl cellulose [45, 46]; $La_{0.7}Sr_{0.3}MnO_3$ films deposited by a magnetron sputtering technique on different substrates [47]; K-doped manganite oxide prepared by magnetron sputtering [48]; $La_{0.7}Ca_{0.3-x}K_xMnO_3$ coatings with $\Delta\varepsilon$ values up to 0.46 [49]; and K-doped $La_{0.7}Ca_{0.3-x}K_xMnO_3$ (LCKMO, $x = 0.05$, 0.10, 0.15, and 0.20) synthesized by the conventional solid reaction method [50].

Several studies have used vanadium dioxide (VO_2) as another thermochromic material. Multifunction smart coatings for space applications were described based on a passive thin-film structure employing VOn transition metal oxides [51]. Wang et al. fabricated a multilayer film consisted of VO_2, HfO_2, and Ag, and they observed its reversible change of emissivity from 0.13 °C at 30 °C to 0.68 °C at 80 °C [52]. Taylor et al. proposed a VO_2-based Fabry–Perot emitter for dynamic radiative cooling applications [53], and they achieved a total emittance increase from 0.14 at room temperature to 0.60 at 100 °C [54]. They also fabricated a VO_2-based nanophotonic variable emissivity coating for cold space environments [55]. Ueno et al. proposed a multifunctional passive thermal control device that focuses not only on the variable emissivity characteristics of VO_2 but also on the changes in thermal conductivity and specific heat in the vicinity of the phase transition temperature [56].

There are several examples of research using electrochromic materials aimed at spacecraft temperature control. A variable emittance panel for a nanosatellite built with thin films of the electrochromic material tungsten oxide (WO_3) deposited by sputtering was proposed by Larsson et al. in 1999 [57]. They measured the IR emissivity modulation ($\Delta\varepsilon$) of WO_3 films deposited on indium-tin-oxide (ITO)-coated glass, and they observed $\Delta\varepsilon = 0.12$ and 0.3 for crystalline and amorphous films, respectively. Hutchins et al. determined the dependence of the IR spectral optical constants of electrochromic WO_3 thin films from their spectrophotometric measurements of the transmittance and reflectance of variable IR reflectance devices [58]. Significant IR electrochromism using conducting polymers (CPs) with applications in thermal control panels for spacecraft was reported by Chandrasekhar et al. [59]; the measured emissivity variations ranged from 0.32 to 0.79 and the solar absorptivity ranged from 0.39 to 0.79 at operating temperatures from − 35 °C to + 85 °C.

Bergron et al. developed variable absorptivity and variable emissivity devices made of Cu deposited on IR-transparent substrates using Mylar® (UV/vis/near-IR) and ZnSe (long-wavelength IR) [60], as illustrated in Fig. 9. They obtained the maximum absorptivity modulation of 0.32 and the maximum emissivity modulation of 0.53. More recently, dodecylbenzene sulfonate acid (DBSA)-doped polyaniline (PANI) films were synthesized in situ on a Au/porous flexible substrate by electrochemical deposition, and the $\Delta\varepsilon$ values of this IR electrochromic device were 0.183 (wavelength range 3–5 μm), 0.388 (8–12 μm), and 0.315 (2.5–25 μm) depending

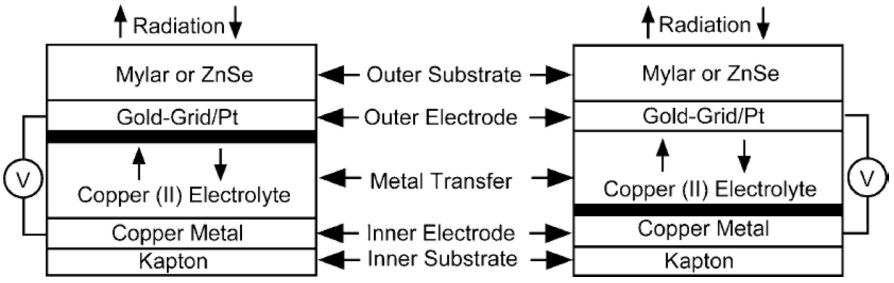

Fig. 9 Cross-section and switching mechanisms of the variable absorptivity and emissivity devices. Reprinted with permission from [60], Copyright (2022) American Chemical Society

on the wavelength range [61]. Zhang et al. reported $HClO_4$-doped PANI porous films which showed modulation of the emittance variation from 0.735 to 0.316 ($\Delta\varepsilon = 0.419$) [62].

DBSA-doped PANI films electrodeposited on both sides of a gold-plated nylon porous membrane were investigated by Song et al.; they obtained the IR emission modulation of 0.43 and 0.40 at the wavelength ranges of 8–14 μm and 2.5–25 μm, respectively [63]. The same group also described a PANI/Au composite film designed with a neoteric mosaic structure [64]. Teissier et al. developed flexible all-polymer electro-emissive devices for the thermal control of satellites by using a semi-interpenetrating network of poly(ethylene oxide) and poly(3,4-ethylenedioxythiophene) (PEO/PEDOT) [65].

Other variable emissivity devices applying microelectromechanical system (MEMS) technology for nano- and micro-spacecraft applications have been reported by NASA's research groups since the early 2000s [66–75]. More recently, Sung-Hyon et al. proposed a MEMS variable emissivity radiator based on the polarity change of electrodes by using the electric charge of silicon beads whose effective emissivity at the closed mode was 0.63 and 0.31 at the open mode [76, 77]. A MEMS radiator with a diaphragm spring structure was developed by Ueno et al. [78, 79], and they reported that by changing the gap between the diaphragms with low-voltage switching, the heat flux at ON–OFF was notably changed.

4.2 RF-Transparent and/or Tunable α_S/ε_H Thermal Control Materials

Spacecraft on orbit internally generate electronics waste heat of several hundred watts to a few kilowatts. On the ground, the internal power dissipation can be cooled by convection or a refrigerator and released into the atmosphere. However, since the space environment is a vacuum, the internal power dissipation must be rejected to space only by radiation, as explained in Sect. 4. In order to keep the temperature of the spacecraft low, it is necessary to reduce the incident energy input from the sun and to increase the total hemispherical emissivity of the radiator. An optical solar reflector (OSR) or a second-surface mirror (SSM), which have been conventionally used for this purpose, have a structure in which a metal is vapor-deposited on the back surface of glass, as illustrated in Fig. 10a [10]. The IR radiation is emitted by using the IR characteristics of the glass itself ($\varepsilon_H = 0.8$ depending on the glass thickness), and the solar radiation transmitted through the glass is reflected by the metal on the back surface ($\alpha_S = 0.15$). Quartz glass, Teflon™, and polyetherimide, which each has high total hemispherical emissivity, have been used as the radiator base material. These materials are transparent to solar radiation, and with the depositing of a silver or aluminum thin film on their back surface, they reflect solar radiation and achieve low solar absorptivity. An OSR has provided the radiator function by two different composites of quartz glass or Teflon and a thin metallic film.

However, quartz glass is heavy, Teflon is vulnerable to radiation, and polyetherimide is vulnerable to ultraviolet radiation; the use of these base materials as lightweight and space environment-resistant radiators in unconventional long-term interplanetary missions should thus be avoided. In addition, in the case of an inner

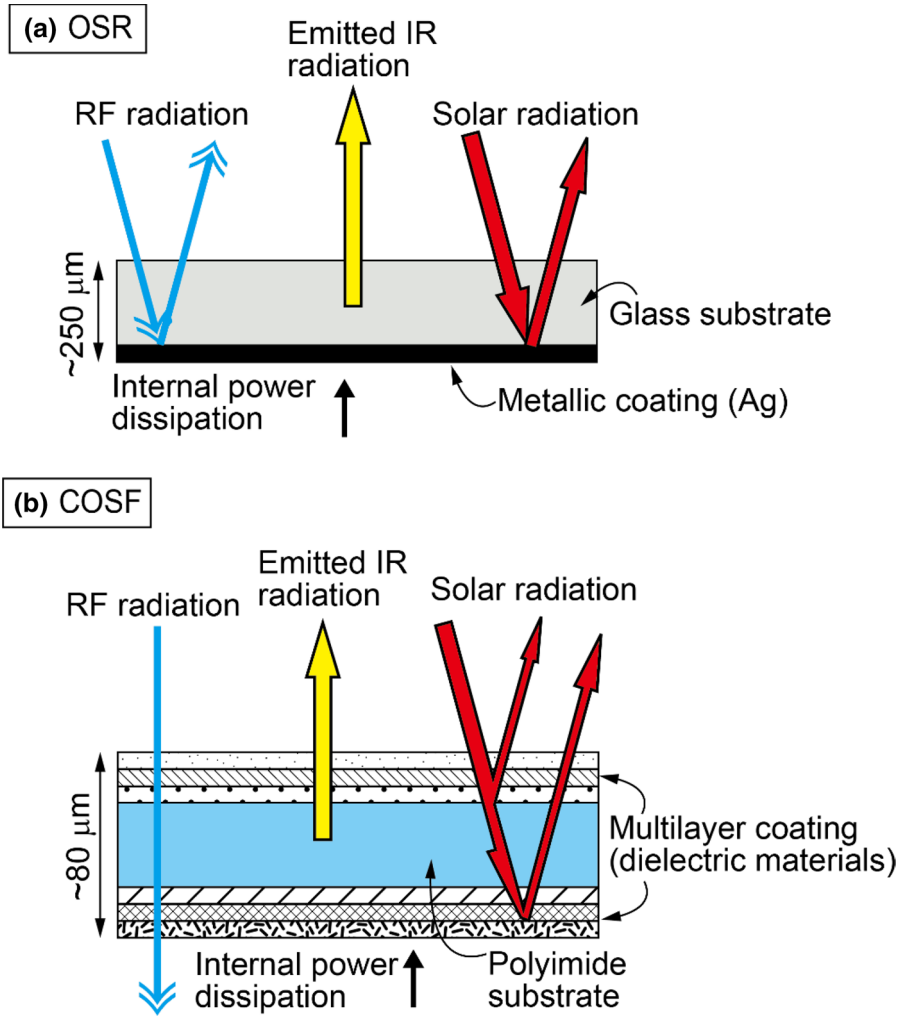

Fig. 10 (a) The structure of a conventional optical solar reflector (OSR) and (b) the basic concept of a controlled optical surface film (COSF)

planetary orbit, it is necessary to install radiators not only on the structure of the spacecraft but also on the antenna, and the radiator needs not only to reject heat but also to transmit radiofrequency (RF) energy. The thermal control material used for the path of the antenna beam must be almost 100 % transparent to RF. A conductive metal that is not transparent to RF therefore cannot be used for the thermal control material that covers the antenna. Ge-coated Kapton® has been used as an RF-transparent antenna cover, but this material has high solar absorptivity ($\alpha_S = 0.45$) and cannot be used for inner planetary orbits with high solar radiation intensity [80]. It is important to note that, to the best of our knowledge, no studies of this topic have been published, other than the papers introduced below.

To deal with the above-mentioned problems, radiators with the following novel functions have become necessary. (1) It has RF transparency and tunable α_S/ε_H (or an α_S/ε_H smaller than that of an OSR) at the same time, (2) it has high space environmental resistance, and (3) it is lightweight and has flexibility that can be easily applied to curved surfaces. Tachikawa et al. first proposed a unique RF-transparent radiator film that has all of the above functions: they called this new thermal control mirror "controlled optical surface film (COSF)" [80–82]. As shown in Fig. 10b, a polyimide film (UPILEX®-S) with a large ε_H value that is lightweight and has both space environmental resistance and RF transparency is used as the base material, and an RF-transparent dielectric multilayer film is used for the surface. In this radiator, short-wavelength solar radiation is reflected by the dielectric multilayer film that allows RF transmission on the front surface, and long-wavelength solar radiation transmitted through the polyimide is reflected by the dielectric multilayer film on the back surface. At the same time, the radiator as a whole maintains high total hemispherical emissivity.

The biggest challenge is how to optimally design the multilayer film of such an RF-transparent radiator. Although there are many studies and standard methods for designing ordinary narrow-band optical interference filters that block or transmit specific wavelengths [83–85], there has apparently been no research about optimizing the optical constants refractive index $n(\lambda)$ and the extinction coefficient $k(\lambda)$ of multilayer films in such a wide band (0.25–100 μm) for ground uses other than space thermal control use. A method for designing a COSF with the proposed film structure (Fig. 10b) by using a genetic algorithm (GA) has been developed [30, 80]. Figure 11a presents the design flowchart of a COSF created with the use of a GA corresponding to the film structure; the multiple reflection at the boundary surface between the mth and $(m+1)$th layers in the multilayer film on the substrate is described in Fig. 11b. The equations used to calculate the solar absorptivity α_S and the total hemispherical emissivity ε_H of the radiator from the optical constants (n_m, k_m)and the film thickness d_m of the constituent mth layer film materials are described below [86]. The spectral reflectance at the boundary surface with the incident angle Θ between the mth and $(m-1)$th layers can be recursively expressed as:

$$R'_m(\lambda,\theta)=\frac{r_m+R'_{m-1}(\lambda,\theta)\exp(-i\eta_m)}{1+r_mR'_{m-1}(\lambda,\theta)\exp(-i\eta_m)}, \tag{4}$$

where $\eta_m=4\pi\hat{n}_m d_m\cos\theta_m/\lambda$; $\hat{n}_m=n_m-ik_m$ is the complex refractive index of the mth layer; and r_m represents the Fresnel coefficient. The spectral reflectance of the multilayer film is thus given as follows:

$$R(\lambda,\theta)=\frac{\left|R'_{S(m+1)}\right|^2+\left|R'_{P(m+1)}\right|^2}{2}, \tag{5}$$

where $R'_{S(m+1)}$ and $R'_{P(m+1)}$ are the s-polarization reflectance and p-polarization reflectance of the surface of the multilayer film, respectively. The temperature dependence

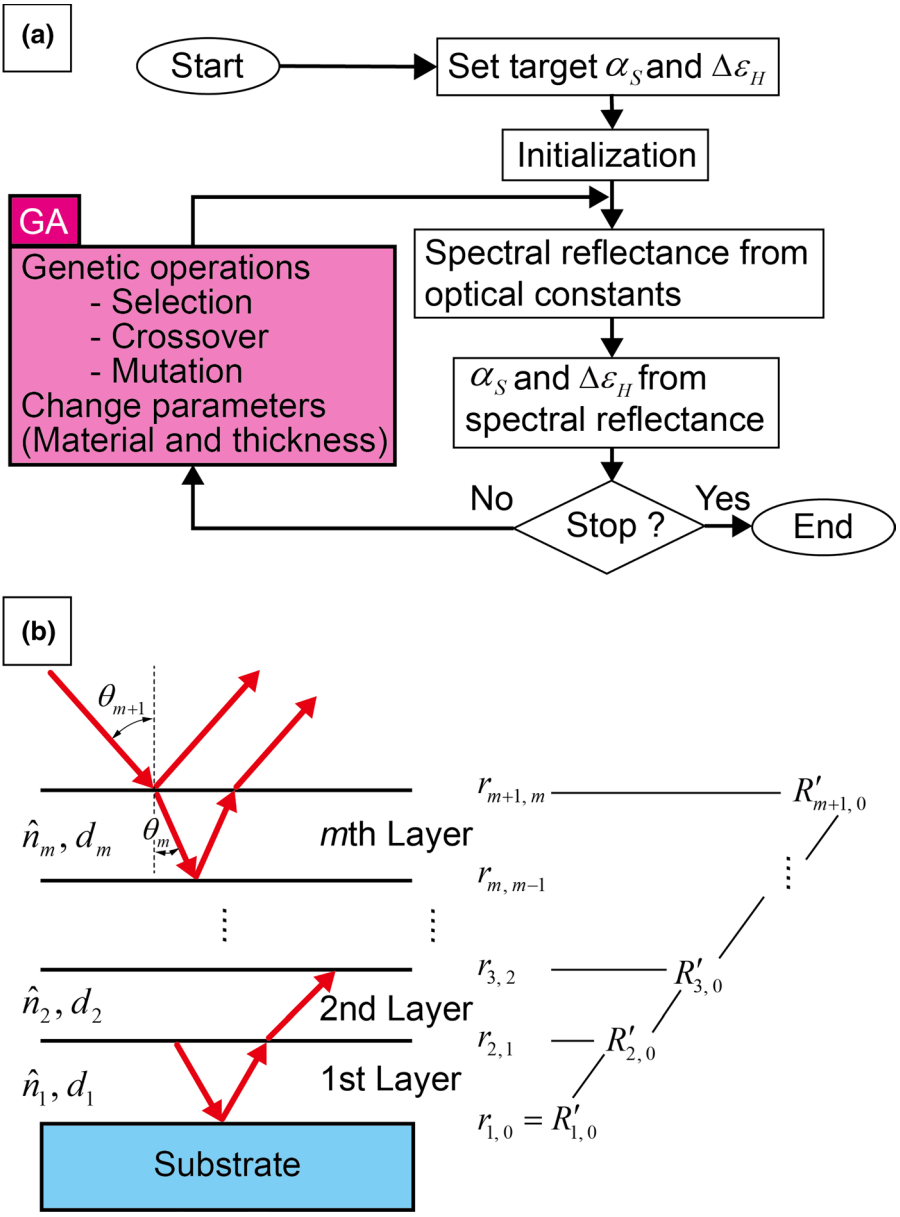

Fig. 11 (a) Design flowchart of a controlled optical surface film (COSF) using a genetic algorithm (GA) and (b) the multiple reflections in a multilayer film to calculate the spectral reflectance

of the total hemispherical emissivity ε_H is calculated by the integration of the spectral reflectance in the wavelength range from 0.25 μm to 100 μm, expressed as:

$$\varepsilon_H(T) = \frac{\int_0^{\pi/2}\int_{0.25}^{100}[1-R(\lambda,\theta)]i_b(\lambda,T)\cos\theta\sin\theta d\lambda d\theta}{\int_0^{\pi/2}\int_{0.25}^{100} i_b(\lambda,T)\cos\theta\sin\theta d\lambda d\theta}, \tag{6}$$

where T is the absolute temperature of the sample and $i_b(\lambda,T)$ is the spectral intensity of blackbody radiation at temperature T. The 0.25- to 100-μm spectral region contained approx. 97.8 % of the emissive power at 173.15 K and > 99.7 % at 373.15 K, which are an acceptable approximation for engineering applications. The solar absorptivity α_S is calculated by the integration of the spectral reflectance in the wavelength range from 0.25 μm to 2.5 μm:

$$\alpha_S = \frac{\int_{0.25}^{2.5}[1-R(\lambda,\theta)]J_S(\lambda)d\lambda}{\int_{0.25}^{2.5} J_S(\lambda)d\lambda}, \tag{7}$$

where $J_S(\lambda)$ indicates the spectral solar radiation intensity; the spectral region between 0.25 μm and 2.5 μm covers approx. 96 % of the solar radiation intensity. The inconsistency of the maximum wavelength of integration in the case of the total hemispherical emissivity in Eq. 6 is due to experimental constraints, but this is sufficient for outer planetary orbits where the solar radiation intensity is relatively low.

Here, we will not go into the details of designing a dielectric multilayer film with a GA [80]; we will simply provide a comparison of the calculation results of the optimum design with the experimental results of the multilayer film radiator created according to the design. Figure 12 illustrates the comparison of designed values with the measured spectral reflectance and the total hemispherical emissivity together with the RF transmittance of a COSF and other conventional thermal control materials [80]. The substances used for the multilayer film were Ta_2O_5, TiO_2, Ge, SiO_2, and Si, with a maximum of 42 layers and an overall thickness of approx. 80 μm. With this comparison, it became clear that the solar absorptivity and the total hemispherical emissivity of a COSF can be independently designed and produced to any desired values with almost 100 % transparency to RF. In addition, one of the major merits of a COSF as a radiator is that the α_S can be set to 0.1 or less (an α_S/ε_H value smaller than that of an OSR), and thus, the COSF can be applied to orbits with high solar radiation intensity.

At the same time, as explained above in Sect. 3, new thermal control materials must be degradation-tested in a space environment. For an on-orbit verification test, the developed COSFs were mounted on the International Space Station (ISS) and exposed to the ISS orbit space environment from 2016 to 2020, as shown in Fig. 13. There were no detectable changes in the solar absorptivity of the COSF samples recovered from the 1-year, 2-year, and 3-year exposure tests.

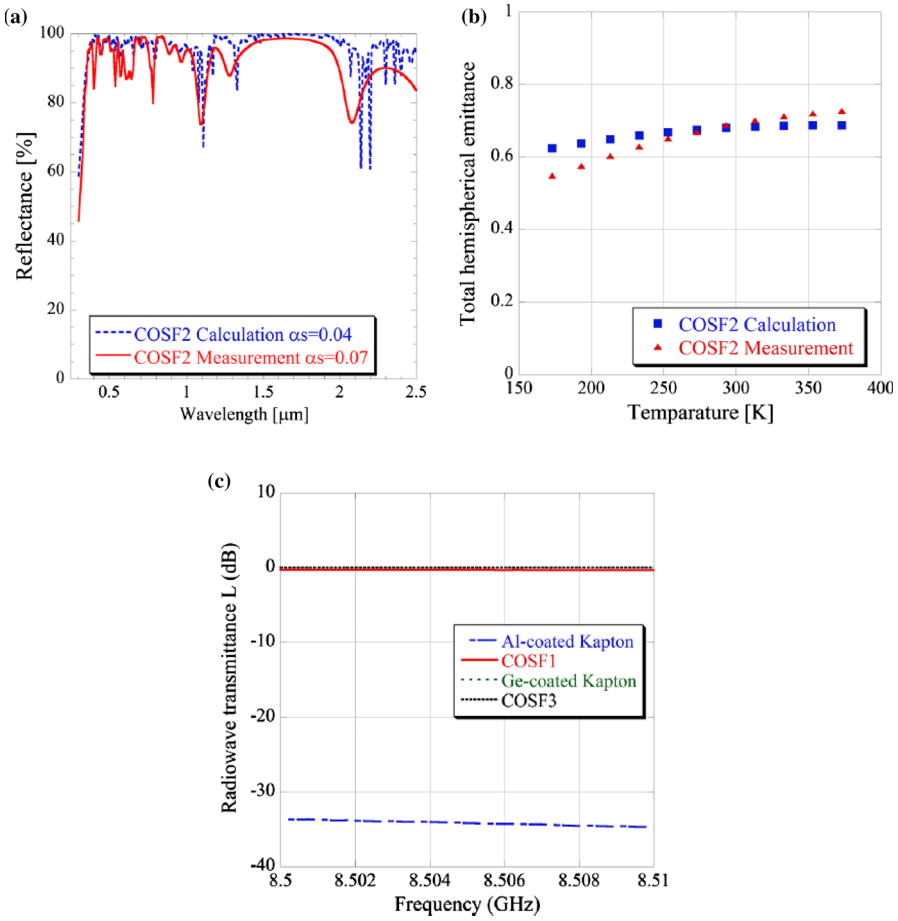

Fig. 12 Comparison of designed values with measured (a) spectral reflectance in the wavelength range 0.26–2.5 μm, (b) total hemispherical emissivity, and (c) RF transmittance of a COSF at X-band (used for radar and satellite communication) and other conventional thermal control materials including Al-coated Kapton and Ge-coated Kapton. Reprinted by permission from AIAA [80], Copyright (2022)

4.3 Passive Re-deployable Radiator with Advanced Materials

The variable emissivity materials and RF-transparent and tunable α_S/ε_H materials introduced in the previous two sections are passive space thermal control materials that can replace the conventional louvers and OSR, respectively, at the very least; they possess the additional benefits of being extremely lightweight with zero energy consumption. On the other hand, these materials could be considered for installation in the structure of a relatively small satellite with heat rejection up to several hundreds of W. When the internal heat generation is large, the required amount of heat rejection cannot be achieved. Deployable radiators are thus suitable to base heat rejection of up to several kW by expanding the radiator area of the spacecraft to the

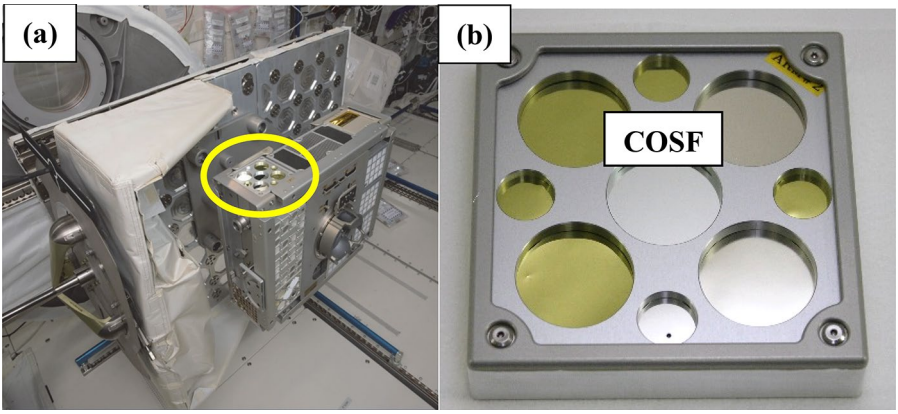

Fig. 13 (a) The Advanced Radiator Material (ARM) module mounted on the Exposed Experiment Handrail Attachment Mechanism (ExHAM) at the Japanese Experiment Module "Kibo" on the International Space Station (ISS), and (b) the COSF (30-mm-dia. with $\varepsilon_H = 0.77$ and $\alpha_S = 0.07$measured on the ground) under a degradation test on the ISS orbit carried out from 2016 to 2020 (the exposed material for the first year was recovered in September 2017 and others were recovered in 2021). Reprinted with courtesy of JAXA

outside; these radiators have been widely employed [87]. The deployable radiators have also been used in combination with fluid loops, but this configuration has the drawbacks of being complex and heavy, and requiring extra heater power because of the large amount of heat rejection (loss) at low temperatures. In this context, there is a demand for a reversible deployable radiator that can expand the radiator area to increase heat rejection from the spacecraft at high temperatures and fold the radiator area at low temperatures to suppress heat rejection. To reduce the weight and power consumption, a passive mechanism using the functional characteristics of advanced materials is also desirable. In this section, we will review the research examples of radiators with heat rejection and heat retention functions, and we introduce a study examining the potential of fully passive re-deployable radiators with no energy consumption.

The concept of a deployable/stowable radiator has been around since the 1970s: Cox et al. proposed a radiator that can be deployed and stowed by expanding the radiating surface using volume expansion due to the evaporation of fluid [88]. Their group was ready to develop an engineering model for the Space Shuttle experiment, but the model was never demonstrated on orbit. Since then, no research has been conducted on reversible deployable radiators. In recent years, however, research concerning reversible deployable radiators has been active toward the development of radiators for ultra-small satellites that have strict restrictions on the heat rejection area, mass, and power resources, and to meet the demand for deployable radiators that can respond to both the high- and low-temperature environments encountered in planetary exploration missions.

Figure 14 shows a new inflatable radiator that is comprised of the combination of a fluid loop composed of a highly thermal-conductive pyrolytic graphite and a flexible tube, developed by Groot et al. [89]. A breadboard model was constructed for

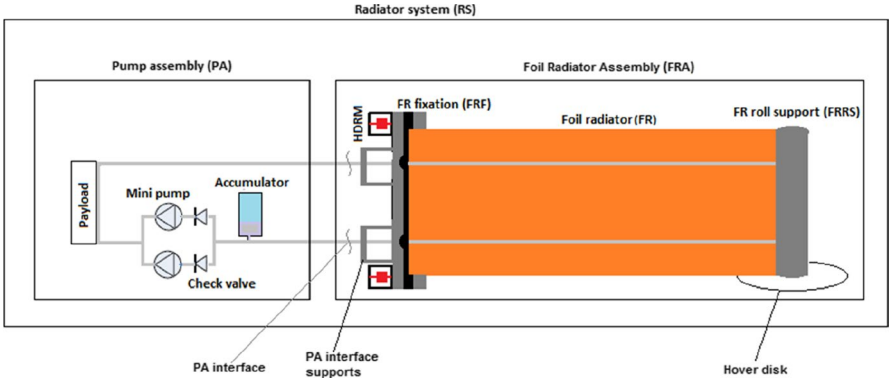

Fig. 14 A system overview of an inflatable radiator [89]

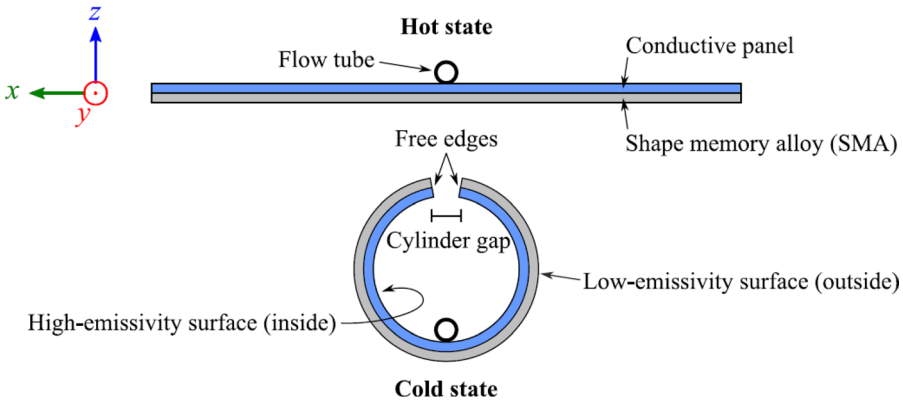

Fig. 15 A conceptual illustration of the morphing radiator design. Reprinted from [90], Copyright (2022), with permission from Elsevier

the validation of the functional design. Bertagne et al. proposed a morphing radiator that uses a shape-memory alloy with high thermal conductivity as a fin and a flow path of a single-phase fluid loop as a heat transfer medium [90]. As illustrated in Fig. 15, the underlying design concept is that the fins will expand completely to promote heat rejection at high temperatures, and the radiator will have a cylindrical shape at low temperatures in order to reduce the view factor for outer space on surfaces with high emissivity. Lutz et al. developed a novel vapor-pressure-driven variable-view-factor and deployable radiator that uses two-phase heat transfer with geometric features that reversibly adjust the view factor in response to internal pressure in the radiator with temperature variations [91].

A steerable spacecraft radiator with an O-ring rotary joint capable of operating with anhydrous ammonia as a working fluid was proposed by Thurn et al. [92]. The above-mentioned research concerns radiators that can be reversibly expanded and stowed by using the pressure change of the fluid, but the structure becomes

complicated because the volume change of the fluid is used as the driving force. There are also reversible deployable radiators that do not use fluids. A radiator structure, in which four aluminum alloy plates are connected by a flexible thermal strap, plus a radiator that can be actively expanded and collapsed by combining with an actuator subsystem using electric power were demonstrated by Mulford et al. [93]. A passively actuated radiator with four triangular fins for microsatellites was proposed by Cannon et al. [94]. By using bimetallic coils as the actuator, zero power consumption and a simple structure are realized.

Nagano et al. [95, 96] focused on the use of a pyrolytic graphite sheet (PGS), which has characteristics of high thermal conductivity, light weight, and flexibility. Prior to the conceptual design of the thermal control device, they measured

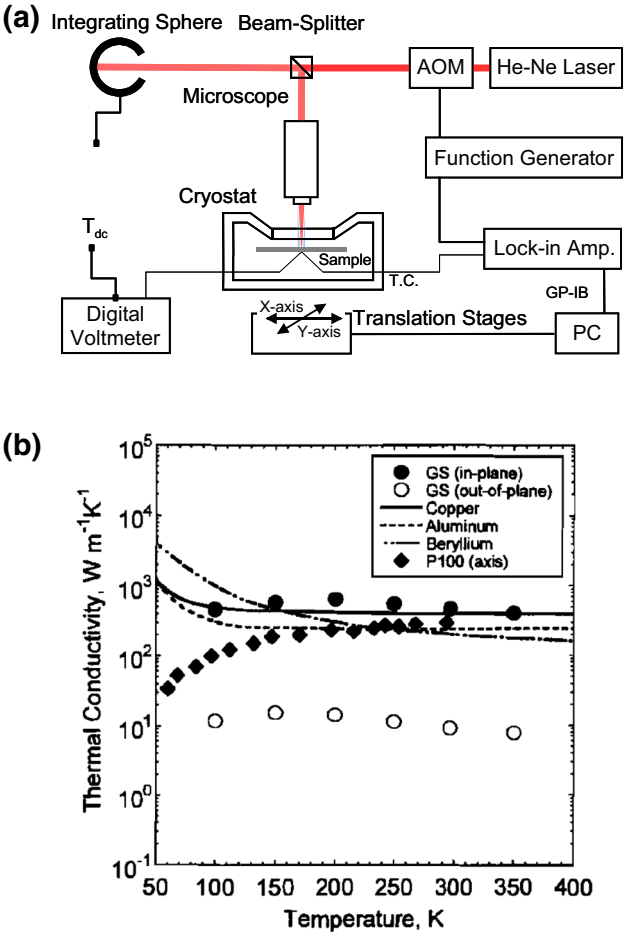

Fig. 16 (a) Laser-heating AC calorimetric method to measure the high and anisotropic thermal conductivity of a pyrolytic graphite sheet (PGS) and (b) experimental thermal conductivity results. Reprinted by permission from AIAA [96], Copyright (2022)

its thermal conductivity, total hemispherical emissivity, and solar absorptivity and evaluated the effect of proton irradiation on the thermal conductivity considering the purpose of space applications [97]. Figure 16 illustrates the laser-heated AC calorimeter method for measuring the high and anisotropic thermal conductivity of the PGS, plus the experimental results [96]. By using PGS, which has excellent thermophysical properties as a thermal control material for space use, as a base material, Nagano et al. created a prototype of a passive deployable/stowable radiator, i.e., a reversible thermal panel (RTP) [98], which is composed of flexible high-thermal-conductive materials and a passive reversible actuator. The RTP changes its function from a radiator to a solar absorber by deploying/stowing the reversible fin upon changes in the heat rejection and thermal environment. The conceptual design and a detailed cross-sectional view of the RTP are illustrated in Fig. 17. Observations of the RTP's heat rejection performance in an autonomous thermal control test on the ground together with a comparison of the experimental and numerical analysis results were carried out [99]. Currently, the RTP is being fabricated and tested toward its installation in the deep space exploration satellite "Demonstration and Experiment of Space Technology for

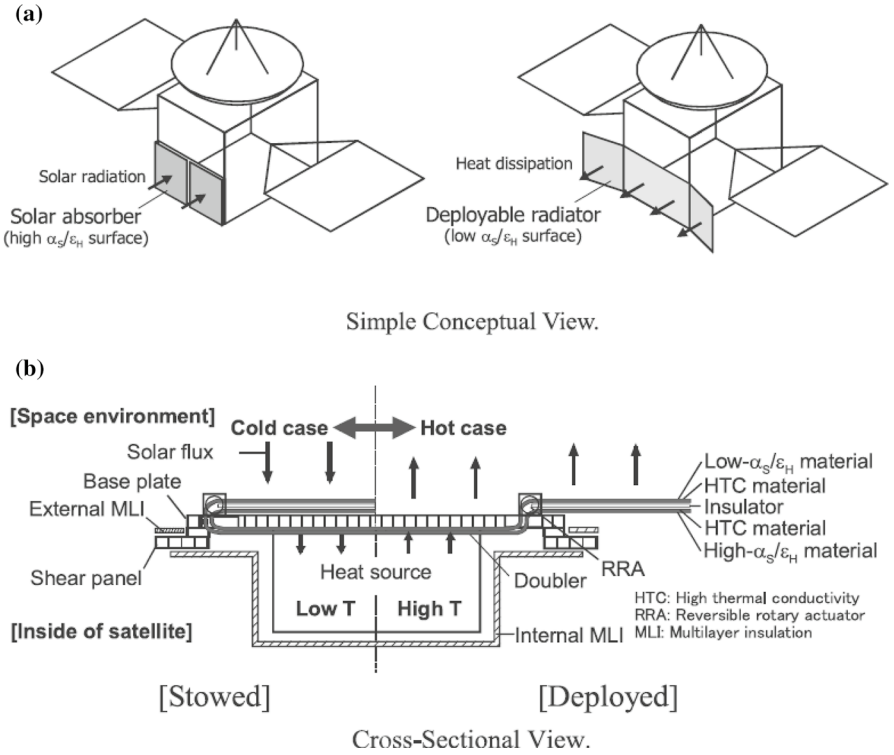

Fig. 17 (a) A Conceptual design of a reversible thermal panel (RTP) utilizing characteristic thermophysical properties of a PGS and (b) the detailed structure of the RTP. Reprinted by permission from AIAA [98], Copyright (2022)

INterplanetary voYage, Phaethon fLyby and dUst Science" (DESTINY +) being developed by JAXA [100].

5 Insulation

A spacecraft's insulation system keeps the temperature of the spacecraft structure and on-board equipment within an allowable limit by blocking the heat input due to solar radiation and heat conduction from other equipment, and by blocking heat output from on-board equipment. The on-board equipment that needs to be insulated includes mainly batteries, internal propellant tanks, propellant piping, valve modules, electronic equipment with a small heat capacity, and sensors. Multilayer insulation (MLI) is the most widely used passive thermal control element for space. When used inside a spacecraft, the MLI consists of a stack of 8–15 layers of double-sided aluminum vapor-deposited polyester film that reduces the radiative heat transfer between layers, plus a polyester net that reduces conduction heat transfer between films (Fig. 18a). Regarding the MLI used for the outer surface of a spacecraft, an aluminum-deposited polyimide film that has a different number of layers from the internal MLI and has high heat resistance, radiation resistance, and ultraviolet resistance is generally used for the outermost layer and the innermost layer [12]. The MLI is expected to be used in a vacuum, and its thermal insulation effect is not very high in the atmosphere [10].

In practical insulation systems, it is also important to take into account the seams, joints, fasteners, and edge effects of MLI installation. Schuler et al. developed a unique polymer for use in twisted and braided sewing threads that has excellent space durability compared to other conventional organic polymers for applications in low Earth orbit [101]. Cotoros et al. described the design and modeling of depressurization during a spacecraft launch through X-slits cut into the insulation blanket and Velcro strips taped along the sides [102]. Insulation systems for cryogenic applications in space have also been studied. These systems include aerogel beads as the insulation material in both vacuum and no-vacuum conditions [103], variable density multilayer insulation with different configurations and spacers for cryogenic propellant storage on orbit designed for long-duration missions [104], a composite insulation system of spray-on foam insulation and multilayer insulation/variable density multilayer insulation for cryogenic propellant in space applications [105], electrostatic testing of MLI for in-space cryogenic vehicles to understand the charge build-up that multiple different outer covers would generate in both low-earth orbit and geostationary orbit [106], and an experimental investigation of a combination of a vapor-cooled shield and multilayer insulation [107].

Insulation systems capable of tolerating operating pressures from one atmosphere to a vacuum have been investigated. Mills et al. reported a composite multilayer insulation that is cellular load-responsive and provides better thermal performance in both atmospheric conditions and in the vacuum of space [108]. Johnson et al. demonstrated a hybrid MLI system comprised of load-bearing MLI and traditional MLI [109]. In terms of new materials that differ from traditional MLI, there have been a few experimental studies of discrete polymeric spacers between reflective

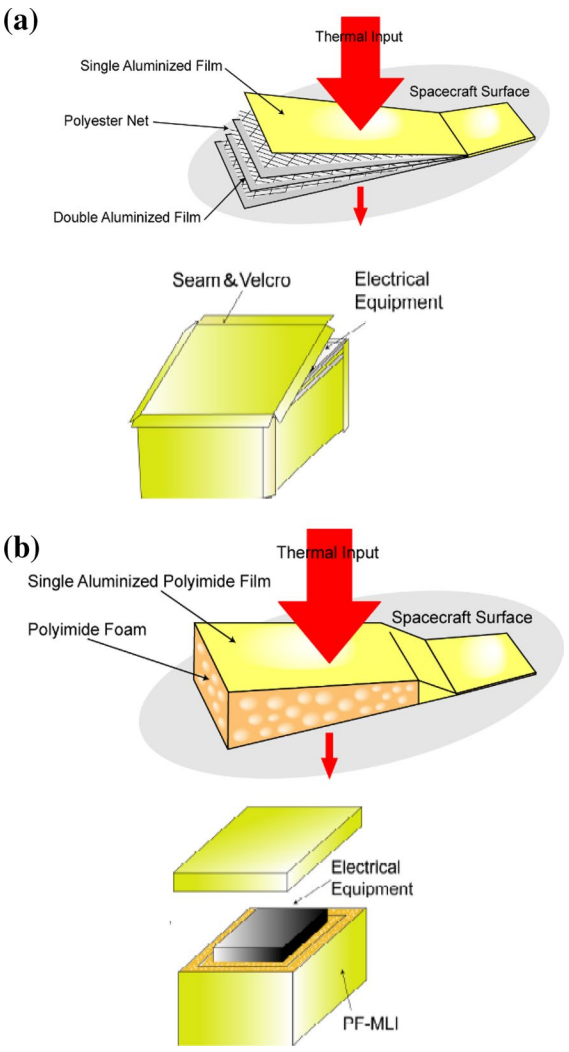

Fig. 18 (a) Typical structure of conventional multilayer insulation (MLI) and its installation, and (b) the structure of polyimide foam (PF)-MLI and its installation without seams or Velcro [116]

layers instead of either Dacron® or silk netting [110], and polyimide foam [111, 112].

There have not been many studies in the EU or the US to further improve the insulation performance of MLI systems. One of the reasons for this may be that in these countries, it is possible to use heat sources with radioisotopes. Other countries including Japan do not have such a heat source, and it is thus necessary to improve the insulation performance of spacecraft that will be in outer planetary orbits with low solar intensity, to the utmost limit. For example, the heat loss through the seams in MLI is not negligible; it has been estimated as 50 % of the total heat loss across the MLI [113]. The quantitative effects of the size and aspects of the hem processing such as overlap, seams, and patches on the thermal performance of MLI are

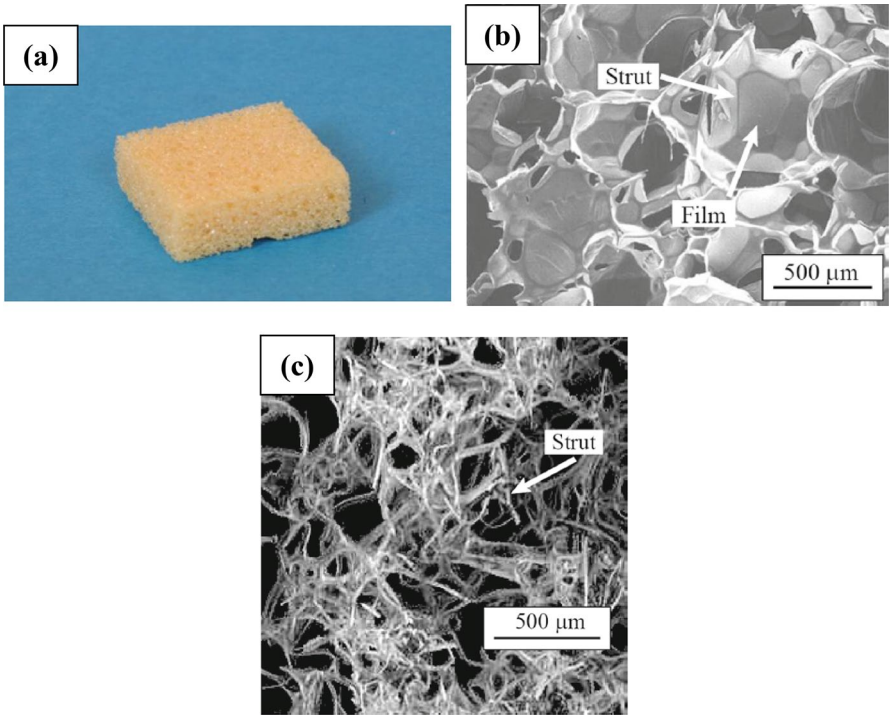

Fig. 19 (a) Bulk appearance of polyimide foam BF301, (b) SEM image of the inner structure of BF301, and (c) 3D X-ray CT image of BF301 taken at BL19B2 of Spring8 at the Japan Synchrotron Radiation Research Institute. Reprinted by permission from Springer Nature [111], Copyright (2022)

Table 2 Porosity and density of each type of polyimide foam determined by X-ray CT images with a dodecahedron model. Reprinted by permission from Springer Nature [111], Copyright (2022)

	BF301	BP101	BP021	BP011
Density ($kg{\cdot}m^{-3}$)	6.67	27.73	117.83	242.63
Porosity (%)	95.4	92.4	73.1	61.7

described in References [114, 115]. Takagi et al. first proposed new thermal insulation composed of polyimide foams (PFs) [116], and multiple aluminized films (PF-MLI) have the potential to be used in outer space as an alternative to conventional MLI as shown in Fig. 18b. In addition, PF has the ability to retain its shape; it is both possible to design seamless insulation containers and to attach insulation to spacecraft panels without Velcro, as illustrated in Fig. 18b [116].

The PF under the trade name of UPILEX® has characteristics of high heat resistance up to 674 K, high durability against protons, electrons, and UV irradiation, high electrical insulation capability, low outgas, and low density. Figure 19 shows the bulk appearance, a scanning electron microscopy image, and a 3D X-ray CT

image of PF. The porosity and density values of each type of PF determined by X-ray CT images with a dodecahedron model are provided in Table 2 [111]. Figure 20 plots the thickness dependence of spectral IR transmissivity of the lowest density PF, BF301. Takagi et al. measured the thermal conductivity of the PF by both the periodic heating method and the guarded hot-plate method (Fig. 21a) in the temperature range of 160–370 K and the density range of 6.67–242.63 $kg{\cdot}m^{-3}$ in both vacuum and atmospheric conditions. The temperature dependence of the effective thermal conductivity of BF301 is shown in Fig. 21b in a comparison with that estimated by means of the lattice Boltzmann method based on a dodecahedron inner microscopic complex structure model which reflects a real 3D X-ray CT image of a PF (Fig. 19c). More recently, Tomioka et al. developed a RF-transparent insulation material (called RT-MLI) [117] by combining polyimide foams with the COSF technology introduced above in Sect. 4.2.

6 Conclusion

The latest advanced passive thermal control materials and devices for spacecraft have been summarized above: variable emissivity thermal control materials and MEMS, RF-transparent and/or tunable solar absorptivity and total hemispherical emissivity thermal control materials, passive re-deployable radiators with advanced materials, and insulation. As the number of manned spacecraft, including commercial spacecraft, increases in the near future, and since the spacecraft are expected to operate with higher energy consumption over longer lifespans than the existing spacecraft, it is increasingly important to develop advanced thermal control technologies that meet the requirements of these spacecraft's unprecedented missions. In order to meet the new needs of unmanned space missions such as planetary

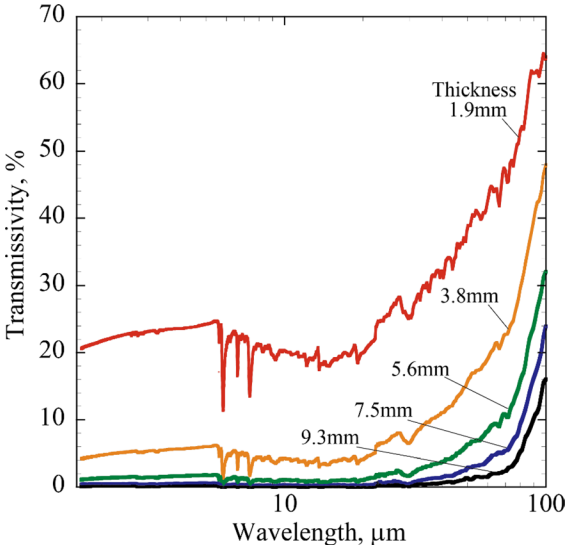

Fig. 20 Thickness dependence of spectral infrared transmissivity of the lowest density polyimide foam BF301. Reprinted by permission from Springer Nature [111], Copyright (2022)

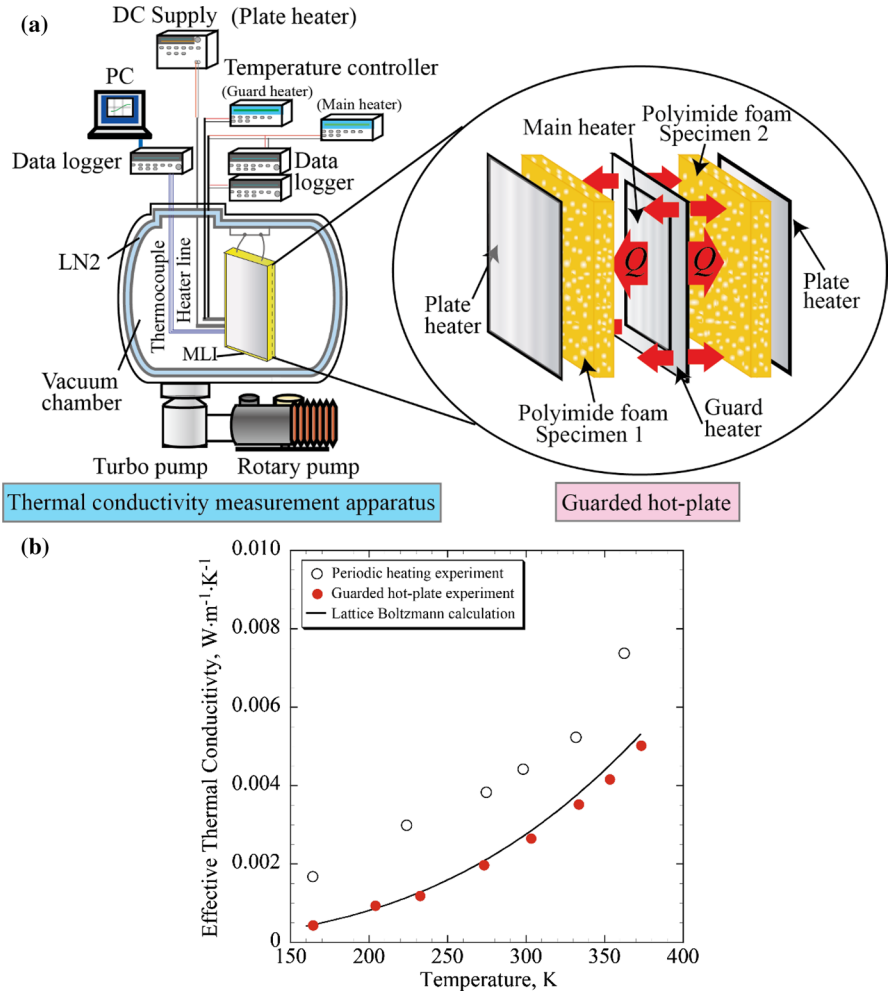

Fig. 21 (a) Thermal conductivity measurement apparatus in a vacuum using the guarded hot-plate method. The guarded hot-plate is suspended in a chamber, and the temperature difference and the heat flux between the plate heater and the main heater are then measured under steady-state conditions. (b) The temperature dependence of the effective thermal conductivity of polyimide foam BF301 in a vacuum determined by the periodic heating and the guarded hot-plate experiments compared with the estimated values using the lattice Boltzmann method. Reprinted by permission from Springer Nature [111], Copyright (2022)

exploration, the further functionalization of radiators and improvements in heat insulation performance will always be required in order to accurately maintain the allowable temperature of spacecraft in low- and high-temperature conditions. If these advances in technology are realized, it will be possible to keep the temperature changes and internal temperature distribution of the spacecraft (due to external heat input) small throughout the mission. As a result, the heater power will be reduced, the number of solar cell panels will be reduced, the mass of the spacecraft will be

reduced, and finally the cost of the entire mission will be reduced and the reliability will be improved.

Regarding radiators, it is necessary to further research and develop radiators that can control the temperature of various parts of the spacecraft more individually and precisely. The creation of a new device that can sharply change the emissivity from 0 to 1 at any desired temperature by further enhancing the function of SRDs is needed. The continued development of COSF technology will enable the development of fine-tuned, custom-made thermal control materials (such as COSFs for antennas) that are tailored to the characteristics of the individual on-board equipment of the spacecraft. In the methods used to adjust the amount of heat rejection by changing the effective heat rejection area of the radiator, it is necessary to further study the application of MEMS technology in a very small area. For larger heat rejection scales, it is essential to develop a passive variable-area radiator with no energy consumption by using the advantages of characteristics such as those of high thermal conductivity materials.

With respect to insulation materials and their installation method, it will always be useful to reduce the energy consumption of spacecraft by improving the performance of new foamed heat-insulating materials such as PF and MLI hem processing (edge finishes such as seams, overlap, and patches). Regarding thermophysical properties research, as the missions to the inner and outer planets advance, it is necessary to develop and improve new advanced measurement techniques with higher accuracy in a wide temperature range of thermophysical properties such as solar absorptivity, total hemispherical emissivity, and thermal conductivity. Thermal control technologies that will be developed in future will not only replace existing technologies but will also offer entirely new options for the thermal design of spacecraft and on-board equipment. Thermophysics in space applications will become even more important in the rapid qualitative and quantitative expansion of space utilization in the near future and in the thermal design of spacecraft with an emphasis on cost and safety.

Acknowledgments The early phase of this work was partially supported by a grant from the Japan Society for the Promotion of Science (JSPS) KAKENHI, No. JP17H01248.

References

1. M. Kaviany, *Principles of Heat Transfer* (Wiley, New York, 2002)
2. Y.A. Çengel, R.H. Turner, *Fundamentals of Thermal-Fluid Sciences* (McGraw Hill, New York, 2001)

3. A. Bejan, *Advanced Engineering Thermodynamics*, 2nd edn. (John Wiley & Sons, New York, 1997)
4. https://sci.esa.int/web/bepicolombo. Accessed 21 January 2022
5. https://www.nasa.gov/content/goddard/parker-solar-probe. Accessed 21 Jan 2022
6. https://www.nasa.gov/mission_pages/newhorizons/overview/index.html. Accessed 21 Jan 2022
7. https://www.hayabusa2.jaxa.jp/en/ . Accessed 21 Jan 2022
8. https://www.nasa.gov/osiris-rex. Accessed 21 Jan 2022
9. https://www.mmx.jaxa.jp/en/. Accessed 21 Jan 2022
10. D.G. Gilmore, ed., *Spacecraft Thermal Control Handbook Volume I: Fundamental Technologies*, 2nd ed. (The Aerospace Press, California, 2002)
11. P. Fortescue, J. Stark, G. Swinerd (eds.), *Spacecraft Systems Engineering*, 3rd edn. (Wiley, England, 2003)
12. A. Ohnishi (ed.), *Thermal Design of Spacecraft* (The University of Nagoya Press, Japan, 2014)
13. R. Siegel, J.R. Howell, *Thermal Radiation Heat Transfer*, 4th edn. (Taylor & Francis, New York, 2002)
14. E.A. Silk, *Introduction to Spacecraft Thermal Control* (Cambridge University Press, UK, 2020)
15. G.L. Stephens, D. O'Brien, P.J. Webster, P. Pilewski, S. Kato, J. Li, Rev. Geophys. **53**, 141 (2015)
16. M. Iwata, A. Ohnishi, H. Hirosawa, F. Tohyama, J. Spacecraft Rockets **38**, 504 (2001)
17. M. Iwata, S. Tachikawa, A. Ohnishi, *in Proc. 11th International Symposium on Materials in Space environment*, Aix en Provence, France (2009)
18. F.P. Lang, H. Wang, S.J. Zhang, J.B. Liu, H. Yan, Int. J. Thermophys. **39**, 6 (2018)
19. K. Shimazaki, S. Tachikawa, A. Ohnishi, Y. Nagasaka, in *Proceedings of 19th Japan Symposium on Thermophysical Properties*, Fukuoka, Japan (1998), p. 75
20. K. Shimazaki, S. Tachikawa, A. Ohnishi, Y. Nagasaka, High Temp. High Press. **33**, 525 (2001)
21. K. Shimazaki, S. Tachikawa, A. Ohnishi, Y. Nagasaka, Int. J. Thermophys. **22**, 1549 (2001)
22. A. Urushibara, Y. Morimoto, T. Arima, A. Asamitsu, G. Kido, T. Tokura, Phys. Rev. B **51**, 14103 (1995)
23. Y. Okimoto, T. Katsufuji, T. Ishikawa, A. Urushibara, T. Arima, Y. Tokura, Phys. Rev. Lett. **75**, 109 (1995)
24. K. Fukuzawa, A. Ohnishi, Y. Nagasaka, Int. J. Thermophys. **23**, 319 (2002)
25. Y. Shimakawa, T. Yoshitake, Y. Kubo, T. Machida, K. Shinagawa, A. Okamoto, Y. Nakamura, A. Ochi, S. Tachikawa, A. Ohnishi, Appl. Phys. Lett. **80**, 4864 (2002)
26. A. Ochi, T. Mori, Y. Shimakawa, Y. Kubo, A. Okamoto, Y. Nakamura, S. Tachikawa, A. Ohnishi, K. Shimazaki, Jpn. J. Appl. Phys. Part 1 Reg. Pap. Short Notes Rev. Pap. **41**, 7263 (2002)
27. Y. Shimakawa, T. Yoshitake, Y. Kubo, T. Machida, K. Shinagawa, A. Okamoto, Y. Nakamura, A. Ochi, S. Tachikawa, A. Ohnishi, Solid State Chem. Inorg. Mater. IV **755**, 419 (2003)
28. S. Tachikawa, A. Ohnishi, A. Okamoto, Y. Nakamura, J. Thermophys. Heat Transf. **17**, 264 (2003)
29. S. Tachikawa, K. Shimazaki, A. Ohnishi, H. Hirosawa, Y. Shimakawa, A. Ochi, A. Okamoto, Y. Nakamura, in *Proceedings of 9th International Symposium on Materials in a Space Environment*, vol. 540 (2003), p. 41
30. K. Shimazaki, A. Ohnishi, Y. Nagasaka, Appl. Opt. **42**, 1360 (2003)
31. K. Shimazaki, A. Ohnishi, Y. Nagasaka, Int. J. Thermophys. **24**, 757 (2003)
32. S. Tachikawa, A. Ohnishi, Y. Nakamura, A. Okamoto, in *Proceedings of 38th International Conference on Environmental Systems*, ICES-2008-01-2152 (2008)
33. T. Shiota, K. Sato, J.S. Cross, N. Wakiya, S. Tachikawa, A. Ohnishi, O. Sakurai, K. Shinozaki, Thin Solid Films **593**, 1 (2015)
34. T. Shiota, Y. Mori, J. Sugiyama, O. Sakurai, A. Nishiyama, N. Wakiya, S. Tachikawa, K. Shinozaki, Thin Solid Films **626**, 154 (2017)
35. S. Tachikawa, A. Ohnishi, Y. Nakamura, A. Okamoto, Trans. Jpn. Soc. Aeronaut. Space Sci. **55**, 367 (2007)
36. Y. Nakamura, A. Okamoto, S. Tachikawa, A. Ohnishi, T. Mori, Y. Shimakawa, in *Proceedings of 17th Conference on Space Engineering* (Japan Society of Mechanical Engineers, Tokyo, Japan, 2008)
37. C.H. Wu, J.W. Qiu, J.B. Wang, M. Xu, L.X. Wang, J. Alloys Compd. **506**, L22 (2010)
38. S.Q. Jiang, X.X. Ma, G.Z. Tang, Z.H. Wang, G. Wang, Z.H. Zhou, J. Rare Earths **29**, 83 (2011)
39. Q. Zheng, W.H. Jiang, Y. Yu, Y.Z. Cao, Y. Yu, L. Mi, L.X. Song, J. Inorg. Mater. **27**, 245 (2012)
40. L. Chen, C.H. Lu, Z.G. Fang, Y. Lu, Y.R. Ni, Z.Z. Xu, J. Phys. D Appl. Phys. **46**, 105302 (2013)

41. S.Q. Jiang, X.X. Ma, G. Wang, G.Z. Tang, Z.H. Wang, Z.H. Zhou, Surf. Coat. Technol. **229**, 76 (2013)
42. Y.J. Shen, C.B. Wang, L. Li, Q. Shen, L.M. Zhang, High-Perform. Ceramics VIII **602–603**, 902 (2014)
43. C.B. Wang, Y.J. Shen, L. Li, J. Mater. Sci. **50**, 5593 (2015)
44. J.F. Liu, F.L. Tang, H.T. Xue, W.J. Lu, Y.D. Feng, J. Magn. Magn. Mater. **390**, 31 (2015)
45. L. Guo, D.S. Fan, Q. Li, Mater. Res. Expr. **3**, 025008 (2016)
46. L. Guo, D.S. Fan, Q. Li, Y.M. Xuan, in *Proceedings of ASME 5th International Conference on Micro/Nanoscale Heat and Mass Transfer*, 2016, vol. 1 (2016)
47. D.S. Fan, Q. Li, P. Dai, Acta Astronaut. **121**, 144 (2016)
48. T. Lu, D.S. Fan, Q. Li, X, Fan. J. Alloys and Compounds **704**, 366 (2017)
49. D.S. Fan, S. Sun, L. Guo, Int. J. Thermophys. **39**, 67 (2018)
50. C.X. Chen, F. Yu, N.N. Xu, D.S. Fan, Ceram. Int. **46**, 15646 (2020)
51. R.V. Kruzelecky, E. Haddad, B. Wong, W. Jamroz, M. Soltani, M. Chaker, D. Nikanpour, X.X. Jiang, *Protection of Materials and Structures from the Space Environment*, ed. by J.I. Kleiman (Springer, Dordrecht, 2006), p. 277
52. X. Wang, Y.Z. Cao, Y.Z. Zhang, L. Yan, Y. Li, Appl. Surf. Sci. **344**, 230 (2015)
53. S. Taylor, Y. Yang, L.P. Wang, J. Quant. Spectrosc. Radiat. Transf. **197**, 76 (2017)
54. S. Taylor, L.S. Long, R. McBurney, P. Sabbaghi, J. Chao, L.P. Wang, Sol. Energy Mater. Sol. Cells **217**, 110739 (2020)
55. S. Taylor, N. Boman, J. Chao, L.P. Wang, Appl. Therm. Eng. **199**, 117561 (2021)
56. A. Ueno, J. Kim, H. Nagano, Int. J. Heat Mass Transf. **166**, 120631 (2021)
57. A.L. Larsson, G. Niklasson, L. Stenmark, in *Proceedings of SPIE 3787, Advances in Optical Interference Coatings* (1999), p. 486
58. M.G. Hutchins, J.M. Gallego, P.E. Milne, D. Jeffrey, I.D. Brotherston, E. O'Keefe, A.J. Topping, N.S. Butt, in *Proceedings of SPIE 4458, Solar and Switching Materials* (2001), p. 138
59. P. Chandrasekhar, G.C. Birur, P. Stevens, S. Rawal, E.A. Pierson, K.L. Miller, Synth. Met. **119**, 293 (2001)
60. B.V. Bergeron, K.C. White, J.L. Boehme, A.H. Gelb, P.B. Joshi, J. Phys. Chem. C **112**, 832 (2008)
61. Y.L. Tian, X.A. Zhang, S.L. Dou, L.P. Zhang, H.M. Zhang, H.M. Lv, L.L. Wang, J.P. Zhao, Y. Li, Sol. Energy Mater. Sol. Cells **170**, 120 (2017)
62. L.P. Zhang, B. Wang, X.B. Li, G.P. Xu, S.L. Dou, X. Zhang, X. Chen, J.P. Zhao, K. Zhang, Y. Li, J. Mater. Chem. C **7**, 9878 (2019)
63. S.S. Song, G.P. Xu, B. Wang, J.X. Gu, H. Wei, Z.C. Ren, L.P. Zhang, J.P. Zhao, Y. Li, Synth. Met. **278**, 116822–116824 (2021)
64. B. Wang, G.P. Xu, S.S. Song, Z.C. Ren, X.B. Li, J.J. Li, X.Q. Xu, W. Zhou, H.B. Li, L.P. Zhang, Y. Li, Electrochim. Acta **390**, 138891–138893 (2021)
65. A. Teissier, J.P. Dudon, P.H. Aubert, F. Vidal, S. Remaury, J. Crouzet, C. Chevrot, Sol. Energy Mater. Sol. Cells **99**, 116 (2012)
66. A.G. Darrin, R. Osiander, J. Champion, T. Swanson, D. Douglas, AIP Conf. Proc. **504**, 803 (2000)
67. D.M. Douglas, T. Swanson, R. Osiander, J. Champion, A.G. Darrin, W. Biter, P. Chandrasekhar, AIP Conf. Proc. **608**, 204 (2002)
68. P. Chandrasekhar, B.J. Zay, G.C. Birur, S. Rawal, E.A. Pierson, L. Kauder, T. Swanson, Adv. Funct. Mater. **12**, 95 (2002)
69. P. Chandrasekhar, B.J. Zay, T. McQueeney, D.A. Ross, A. Lovas, R. Ponnappan, C. Gerhart, T. Swanson, L. Kauder, D. Douglas, W. Peters, G.C. Birur, AIP Conf. Proc. **654**, 157 (2003)
70. M.A. Beasley, S.L. Firebaugh, R.L. Edwards, A.C. Keeney, R. Osiander, in *Proceedings of SPIE 5344, MEMS/MOEMS Components and Their Applications* (2004), p. 98
71. N. Kislov, H. Groger, R. Ponnappan, E. Caldwell, D. Douglas, T. Swanson, AIP Conf. Proc. **699**, 112 (2004)
72. W. Biter, S. Hess, S. Oh, D. Douglas, T. Swanson, in *2005 IEEE Aerospace Conference*, vols. 1–4 (2005), p. 781
73. D.M. Douglas, J.T. Ku, L. Ottenstein, T. Swanson, S. Hess, A. Darrin, AIP Conf. Proc. **746**, 82 (2005)
74. W. Biter, S. Hess, S. Oh, AIP Conf. Proc. **813**, 56 (2006)
75. D. Farrar, D.M. Douglas, T. Swanson, C. Collins, A. Darrin, R. Osiander, AIP Conf. Proc. **880**, 73 (2007)
76. H. Sung-Hyon, S.J. Kang, H.U. Oh, T. Kim, in *2016 IEEE 29th International Conference on Micro Electro Mechanical Systems (MEMS)* (2016), p. 1212

77. T. Kim, S.H. Han, H.U. Oh, J. Microelectromechanical Systems **26**, 113 (2017)
78. A. Ueno, Y. Suzuki, Appl. Phys. Lett. **104**, 093511 (2014)
79. A. Ueno, Y. Suzuki, Int. J. Therm. Sci. **132**, 161 (2018)
80. K. Tomioka, S. Tachikawa, K. Kawahara, Y. Nagasaka, J. Spacecraft Rockets **53**, 1043 (2016)
81. S. Tachikawa, K. Matsumoto, A. Ohnishi, in *Proceedings of 30th Japan Symposium on Thermophysical Properties*, Yonezawa, Japan (2009), p. 4
82. S. Tachikawa, A. Ohnishi, in *Proceedings of 40th International Conference on Environmental Systems*, AIAA Paper 2010-6232 (2010)
83. M. Born, E. Wolf, *Principles of Optics*, 6th edn. (Pergamon Press, Oxford, 1980), p. 61
84. F.A. Jenkins, H.E. White, *Fundamentals of Optics*, 4th edn. (McGraw-Hill, New York, 1976), p. 311
85. M. Kohiyama, *Optical Filter Design* (Optronics Company, Tokyo, 2006)
86. R. Horikoshi, Y. Nagasaka, A. Ohnishi, Int. J. Thermophys. **19**, 547 (1998)
87. T. Tjiptahardja, M. Amidieu, S.V. Oost, B. Mullender, G. Bekaert, J. Mauduyt, W. Supper, in *Proceedings of 30th International Conference on Environmental Systems*, SAE Technical Paper 2000-01-2455 (2000)
88. R.L. Cox and J.W. Leach, AIAA Paper 77-764 (1977)
89. T. Groot, B. Schwieters, R. Benthem, J. Es, A. Pauw, in *Proceedings of 49th International Conference on Environmental Systems*, Boston, USA, ICES-2019-69 (2019)
90. C.L. Bertagne, T.J. Cognata, R.B. Sheth, C.E. Dinsmore, D.J. Hartl, Appl. Therm. Eng. **124**, 986 (2017)
91. A. Lutz, C. Tarau, S. Rokkam, in *Proceedings of 49th International Conference on Environmental Systems*, ICES-2019-211 (2019)
92. A. Thurn, R. Baldauff, R. Sutton, S. Koss, P. Feerst, J. Thermophys. Heat Transf. **29**, 620 (2015)
93. R.B. Mulford, S.D. Salt, L.P. Hyatt, K.S. Meaker, V.H. Dwivedi, M.R. Jones, B.D. Iverson, Appl. Therm. Eng. **178**, 115658 (2020)
94. J.R. Cannon, B.D. Iverson, W. Song, R.B. Mulford, in *Proceedings of Thermal and Fluid Analysis Workshop* (TFAWS 2020)
95. H. Nagano, H. Kato, A. Ohnishi, Y. Nagasaka, Int. J. Thermophys. **22**, 301 (2001)
96. H. Nagano, A. Ohnishi, Y. Nagasaka, J. Thermophys. Heat Transf. **15**, 347 (2001)
97. H. Nagano, A. Ohnishi, Y. Nagasaka, Y.H. Mori, A. Nagashima, Int. J. Thermophys. **27**, 114 (2006)
98. H. Nagano, Y. Nagasaka, A. Ohnishi, J. Thermophys. Heat Transf. **20**, 856 (2006)
99. H. Nagano, A. Ohnishi, Y. Nagasaka, Appl. Therm. Eng. **37**, 347. (2011)
100. Y. Akizuki, H. Nagano, T. Kinjo, K. Sawada, H. Ogawa, T. Takashima, K. Nishiyama, H. Toyota, K. Watanabe, T. Kuratomi, Appl. Therm. Eng. **165**, 114586 (2020)
101. P. Schuler, R. Haghighat, H. Mojazza, High Perform. Polym. **11**, 113 (1999)
102. I. Cotoros, A. Hashemi, in *Proceedings of the ASME Heat Transfer Division 2005*, vol. 2 (2005), p. 55
103. J.E. Fesmire, S.D. Augustynowicz, S. Rouanet, AIP Conf. Proc. **613**, 1541 (2002)
104. B. Wang, Y.H. Huang, P. Li, P.J. Sun, Z.C. Chen, J.Y. Wu, Cryogenics **80**, 154 (2016)
105. J.P. Zheng, L.B. Chen, C. Cui, J. Guo, W.X. Zhu, Y. Zhou, J.J. Wang, Appl. Therm. Eng. **130**, 161 (2018)
106. B.V. Vayner, J.T. Galofaro, W.L. Johnson, IEEE Trans. Plasma Sci. **47**, 3810 (2019)
107. W.B. Jiang, Z.H. Yang, Z.Q. Zuo, P.J. Sun, P. Li, Y.H. Huang, IOP Conf. Ser. Mater. Sci. Eng. **755**, 012153 (2020)
108. G. Mills, S. Dye, A. Kopelove, P. Tyler, in *2015 IEEE Aerospace Conference* (2015)
109. W.L. Johnson, J.E. Fesmire, K.W. Heckle, IOP Conf. Ser. Mater. Sci. Eng **101**, 012015–012017 (2015)
110. W.L. Johnson, K.W. Heckle, J. Hurd, Adv. Cryog. Eng. **1573**, 725 (2014)
111. R. Takagi, S. Tachikawa, T. Ohmura, Y. Nagasaka, Int. J. Thermophys. **35**, 277 (2014)
112. L. Ma, K. Wang, X. Zhang, Z. Zhao, Adv. Astronaut. Sci. Technol. (2021). https://doi.org/10.1007/s42423-021-00091-4
113. S. Okazaki, M. Murakami, H. Kawasaki, T. Yabe, Y. Kanamori, in *38th International Conference on Environmental Systems*, SAE-2008-01-2067, San Francisco, CA (2008)
114. H. Kawasakai, S. Okazaki, M. Murakami, H. Sugita, Y. Kanamori, J. Thermophys. Heat Transf. **28**, 327 (2014)
115. S. Okazaki, H. Kawasaki, M. Murakami, H. Sugita, Y. Kanamori, J. Thermophys. Heat Transf. **28**, 334 (2014)
116. R. Takagi, S. Tachikawa, Y. Nagasaka, in *Proceedings of 63rd International Astronautical Congress*, IAC-12-C2.9.8, Naples, Italy (2012)
117. K. Tomioka, S. Tachikawa, Y. Nagasaka, in *Proceedings of 63rd Space Science and Technology Conference 2019*, Tokushima, Japan (2019), p. 4336

118. https://www.iau.org/public/themes/measuring/. Accessed 21 January 2022

Authors and Affiliations

Sumitaka Tachikawa[1] · Hosei Nagano[2] · Akira Ohnishi[1] · Yuji Nagasaka[3]

[1] Institute of Space and Astronautical Science, Japan Aerospace Exploration Agency, 3-1-1, Yoshinodai, Sagamihara 229-8510, Japan

[2] Department of Mechanical System Engineering, Nagoya University, 1 Furo-cho, Chikusa-ku, Nagoya 464-8603, Japan

[3] Department of System Design Engineering, Keio University, 3-14-1 Hiyoshi, Yokohama 223-8522, Japan